Supplement for

Bioaerosols outcompete dust as dominate immersion-mode-INPs in central Europe and redefine INP parameterizations

Kunfeng Gao[1,†,*], Romanos Foskinis[1,2], Marilena Gidarakou[3], Kalliopi Violaki[1], Guangyu Li[4,‡], Benjamin Tobias Brem[5], Sophie Erb[6], Bernard Clot[6], Marie-José Graber[6], Branko Sikoparjja[7], Predrag Matavulja[8], Dusan Licina[9], Cuiqi Zhang[4], Benoît Crouzy[6], Alexandros Papayannis[1,3], Zamin A. Kanji[4] and Athanasios Nenes[1,10*]

[1]Laboratory of Atmospheric Processes and Their Impacts, School of Architecture, Civil and Environmental Engineering, École Polytechnique Fédérale de Lausanne, Lausanne, Switzerland.
[2]Environmental Remote Sensing Laboratory, School of Architecture, Civil and Environmental Engineering, École Polytechnique Fédérale de Lausanne, Lausanne, Switzerland.
[3]Laser Remote Sensing Unit, Physics Department, National Technical University of Athens, Zografou, Greece.
[4]Department of Environmental Systems Science, Institute for Atmospheric and Climate Science, ETH Zurich, Zurich, Switzerland.
[5]PSI Center for Energy and Environmental Sciences, Villigen PSI, Switzerland.
[6]Federal Office of Meteorology and Climatology MeteoSwiss, Payerne, Switzerland.
[7]Biosense Institute - Research and Development Institute for Information Technologies in Biosystems, University of Novi Sad, Novi Sad, Serbia
[8]Institute for Data Science, University of Applied Sciences North – Western Switzerland, Bahnhofstrasse 6, Windisch, Switzerland
[9]Human-Oriented Built Environment Lab, School of Architecture, Civil and Environmental Engineering, École Polytechnique Fédérale de Lausanne, Lausanne, Switzerland.
[10]Centre for Studies of Air Quality and Climate Change, Institute of Chemical Engineering Sciences, Foundation for Research and Technology Hellas, Patras, Greece.
[†]Present address: Department of Environmental Systems Science, Institute for Atmospheric and Climate Science, ETH Zurich, Zurich, Switzerland
[‡]Present address: Laboratory for Microwave Spatial Intelligence and Cloud Platform, Deqing Academy of Satellite Applications, Deqing, China

Correspondence to: Athanasios Nenes (athanasios.nenes@epfl.ch) and Kunfeng Gao (kunfeng.gao@env.ethz.ch)

S1 Introduction

This supplement document provides additional information and figures to support discussions in the main text.

S2 Information for IN samples

Figure S1 and Table S1 provide the sampling time for untreated samples. Background test and heating treatment conditions for each sample are provided in Fig. S1. The number of each type of sample tested for DRINCZ IN experiments is also provided in Fig. S1. In addition, Table S1 shows the sample number ID used in the main text.

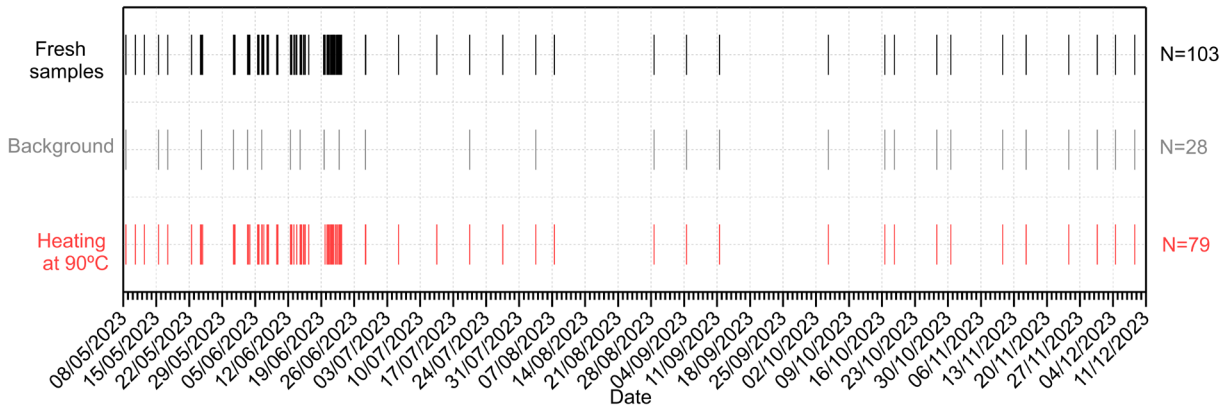

Figure S1. Sampling time, background test and heating treatment for INP samples. N indicates the number of samples.

Table S1. Information for untreated and T90 samples.

Sample Number ID	Sampling start time (UTC+1)	Duration	Background test	Heating at 90°C
0	5/8/2023 13:05	60 min	Yes	Yes
1	5/10/2023 13:22	60 min		Yes
2	5/12/2023 10:55	70 min		Yes
3	5/15/2023 12:09	70 min	Yes	Yes
4	5/17/2023 10:58	60 min	Yes	Yes
5	5/22/2023 11:25	60 min		Yes
6	5/24/2023 8:55	70 min		Yes
7	5/24/2023 14:00	60 min	Yes	Yes
8	5/24/2023 19:05	12 min		
9	5/24/2023 20:02	20 min		Yes
10	5/31/2023 9:00	60 min	Yes	Yes
11	5/31/2023 13:00	60 min		Yes
12	5/31/2023 17:00	20 min		Yes
13	6/3/2023 9:00	30 min	Yes	Yes
14	6/3/2023 11:00	30 min		Yes
15	6/3/2023 13:00	30 min		Yes
16	6/3/2023 18:00	20 min		
17	6/3/2023 19:20	20 min		
18	6/3/2023 20:35	10 min		Yes
19	6/5/2023 12:05	30 min		Yes
20	6/5/2023 16:00	30 min		Yes
21	6/5/2023 19:00	30 min		Yes
22	6/6/2023 8:50	20 min	Yes	Yes
23	6/6/2023 10:59	30 min		Yes
24	6/6/2023 13:36	30 min		
25	6/6/2023 17:00	30 min		
26	6/6/2023 19:45	30 min		Yes
27	6/7/2023 12:10	30 min		Yes
28	6/7/2023 16:00	30 min		Yes
29	6/7/2023 19:45	30 min		Yes
30	6/9/2023 13:45	30 min		Yes
31	6/9/2023 19:00	30 min		Yes
32	6/12/2023 11:25	30 min	Yes	Yes
33	6/12/2023 14:45	30 min		Yes
34	6/12/2023 18:00	30 min		Yes
35	6/13/2023 5:15	30 min		Yes
36	6/13/2023 7:00	30 min		
37	6/13/2023 15:00	30 min		
38	6/13/2023 19:45	30 min		Yes
39	6/14/2023 12:10	30 min	Yes	Yes
40	6/14/2023 16:00	30 min		Yes
41	6/14/2023 19:45	30 min		Yes
42	6/15/2023 5:00	30 min		Yes
43	6/15/2023 8:35	30 min		Yes
44	6/15/2023 14:45	30 min		Yes
45	6/16/2023 8:33	30 min		Yes
46	6/19/2023 12:40	30 min		
47	6/19/2023 15:00	30 min	Yes	
48	6/19/2023 17:00	30 min		
49	6/19/2023 19:00	30 min		Yes
50	6/19/2023 19:45	30 min		

51	6/20/2023 5:00	30 min		Yes
52	6/20/2023 9:10	30 min		
53	6/20/2023 11:20	30 min		Yes
54	6/20/2023 15:00	30 min		
55	6/20/2023 17:00	30 min		Yes
56	6/20/2023 23:00	30 min		Yes
57	6/21/2023 2:00	30 min		Yes
58	6/21/2023 5:00	30 min		Yes
59	6/21/2023 8:35	30 min		Yes
60	6/21/2023 11:00	30 min		
61	6/21/2023 12:00	30 min		
62	6/21/2023 14:05	30 min		Yes
63	6/21/2023 16:00	30 min		
64	6/21/2023 18:00	30 min		
65	6/21/2023 19:45	30 min		
66	6/21/2023 23:00	30 min		Yes
67	6/22/2023 5:00	30 min		Yes
68	6/22/2023 8:35	30 min		
69	6/22/2023 10:00	30 min		
70	6/22/2023 12:00	30 min		Yes
71	6/22/2023 14:00	30 min		
72	6/22/2023 16:00	30 min		
73	6/22/2023 18:35	30 min		Yes
74	6/22/2023 19:10	30 min	Yes	
75	6/22/2023 20:00	30 min		
76	6/22/2023 22:00	30 min		Yes
77	6/23/2023 0:15	30 min		Yes
78	6/23/2023 5:00	30 min		Yes
79	6/23/2023 6:00	30 min		Yes
80	6/23/2023 7:15	30 min		Yes
81	6/28/2023 9:20	30 min	Yes	Yes
82	6/28/2023 10:45	30 min		Yes
83	7/5/2023 9:30	30 min		Yes
84	7/13/2023 13:15	30 min		Yes
85	7/20/2023 11:45	30 min	Yes	Yes
86	7/27/2023 13:07	15 min		Yes
87	8/3/2023 12:45	30 min	Yes	Yes
88	8/7/2023 11:50	30 min		Yes
89	8/28/2023 15:10	15 min	Yes	Yes
90	9/4/2023 12:50	20 min	Yes	Yes
91	9/11/2023 11:50	20 min	Yes	Yes
92	10/4/2023 14:40	10 min	Yes	Yes
93	10/16/2023 13:57	20 min	Yes	Yes
94	10/18/2023 15:20	20 min	Yes	Yes
95	10/27/2023 15:05	20 min	Yes	Yes
96	10/30/2023 14:05	20 min	Yes	Yes
97	11/10/2023 14:35	20 min	Yes	Yes
98	11/15/2023 13:45	20 min	Yes	Yes
99	11/24/2023 15:00	20 min	Yes	Yes
100	11/30/2023 15:40	20 min	Yes	Yes
101	12/4/2023 13:25	20 min	Yes	Yes
102	12/8/2023 15:35	20 min	Yes	Yes

S3 Frozen fraction curves of IN samples and background blanks

Figures S2 and S3 present the frozen fraction curves of all untreated, background and T90 samples. For samples without a corresponding background blank, a fitted curve will be used to correct the background noise following the protocol reported in David et al. (2019). The fit follows the form as below:

Background fit = $\frac{1}{(1+e^{a(T-b)})^c}$,

where *T* is the IN experiment temperature; a, b and c are fitting parameters.

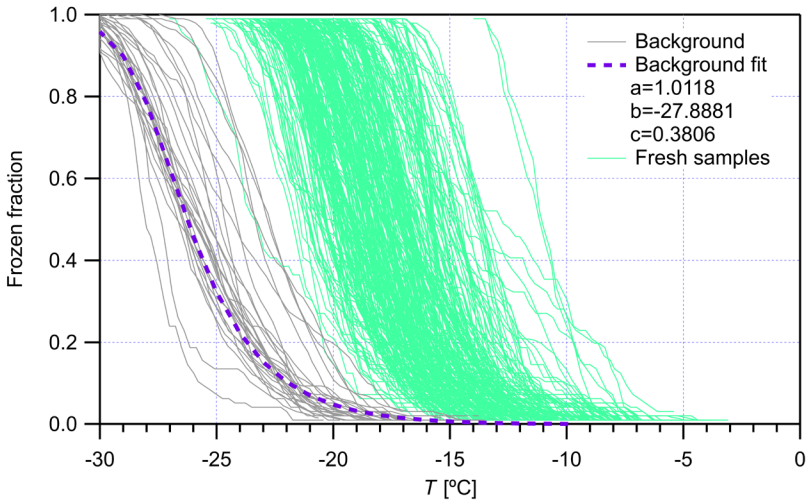

Figure S2. Overview of frozen fractions as a function of temperature obtained with DRINCZ for both untreated and corresponding background samples.

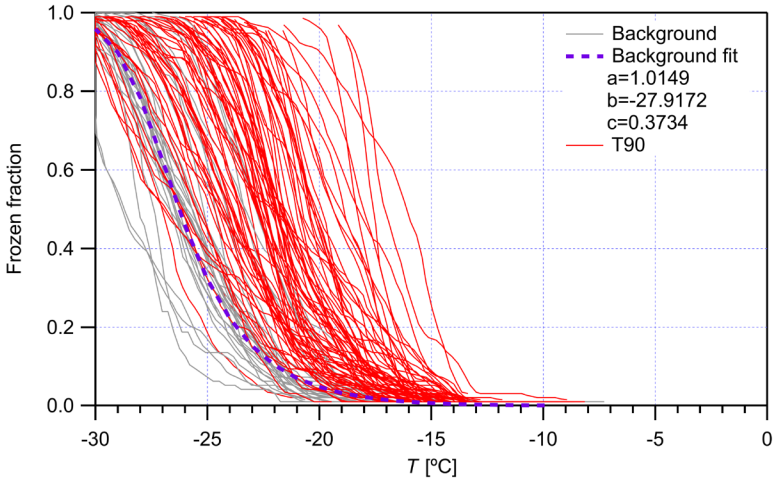

Figure S3. Overview of frozen fractions as a function of temperature obtained with DRINCZ for T90 and corresponding background samples.

S4 ΔT effects on the DRINCZ data processing

Figure S4 shows the N_{INP} results calculated using different ΔT (0.33, 0.50 and 1.0°C) values. It generally shows that a larger ΔT leads to smaller calculated N_{INP} values.

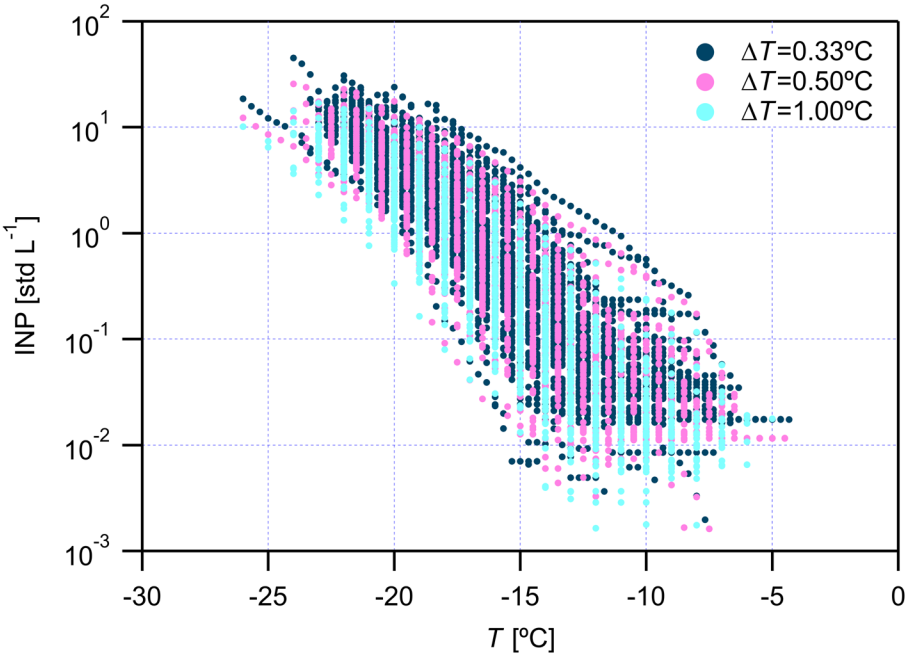

Figure S4. Calculated DRINCZ N_{INP} with different ΔT (0.33, 0.50 and 1.0°C) as a function of T.

S5 Pollen taxa detected by Rapid-E

Rapid-E monitors 11 pollen taxa, mostly at genus level, including Poaceae (family level), Alnus, Betula, Corylus, Taxaceae (family level), Fraxinus, Juglans, Platanus, Populus, Quercus and Salix.

S6 Pollen taxa detected by Hirst

Hirst monitors 48 pollen taxa, including Maple, Amarant, Sweetgum, Ragweed, Sorrel, Mugwort, Mercury, Birch, Nettle, Beech, Common, Umbellifers, Sweet, Yew, Oak, Alder, Spruce, Common, Ginkgo, Grasses, Hornbeam, Buttercup, Hazel, Elder, Hophornbeam, Pine, Daisy, Crucifers, Lime-tree, Larch, Maize, Mulberry, Palm, Poplar, Plane, Rye, Rose, Horse, Sedge, Fir, Elm, Walnut, Plantain, Willow, Miscellaneous, Cedar, Cypress and Olive.

S7 Comparison of PERCILES N_{INP} values against previous field studies in the Alpine region

Figure S5 compares N_{INP} values observed in this study with the selected reference measurements. In general, our N_{INP} range measured N_{INP} range lies in the global envelop range reported by Petters and Wright (2015). Our N_{INP} values increase with decreasing T and approximately spread within a range of one order of magnitude at a fixed T. In comparison to previous field studies in the Alpine region (Wieder et al., 2022; Mignani et al., 2021; Conen et al., 2022; Lacher et al., 2021), our N_{INP} range shows the largest values. This is because our N_{INP} observations were mainly for samples collected in the later spring, summer and autumn and only a few samples were collected during the winter (see Table S1), during which intensive pollen seasons were prevalent. Also, our sampling site was closer to vegetated area at a lower altitude (491 m a.s.l.) compared to the other sites at higher altitudes (>1631 m a.s.l.) close to a mountain top (Wieder et al., 2022; Mignani et al., 2021; Conen et al., 2022; Lacher et al., 2021). This is in agreement with a recent study reporting decreasing N_{INP} values with increasing sampling height in the atmosphere (Gao et al., 2024).

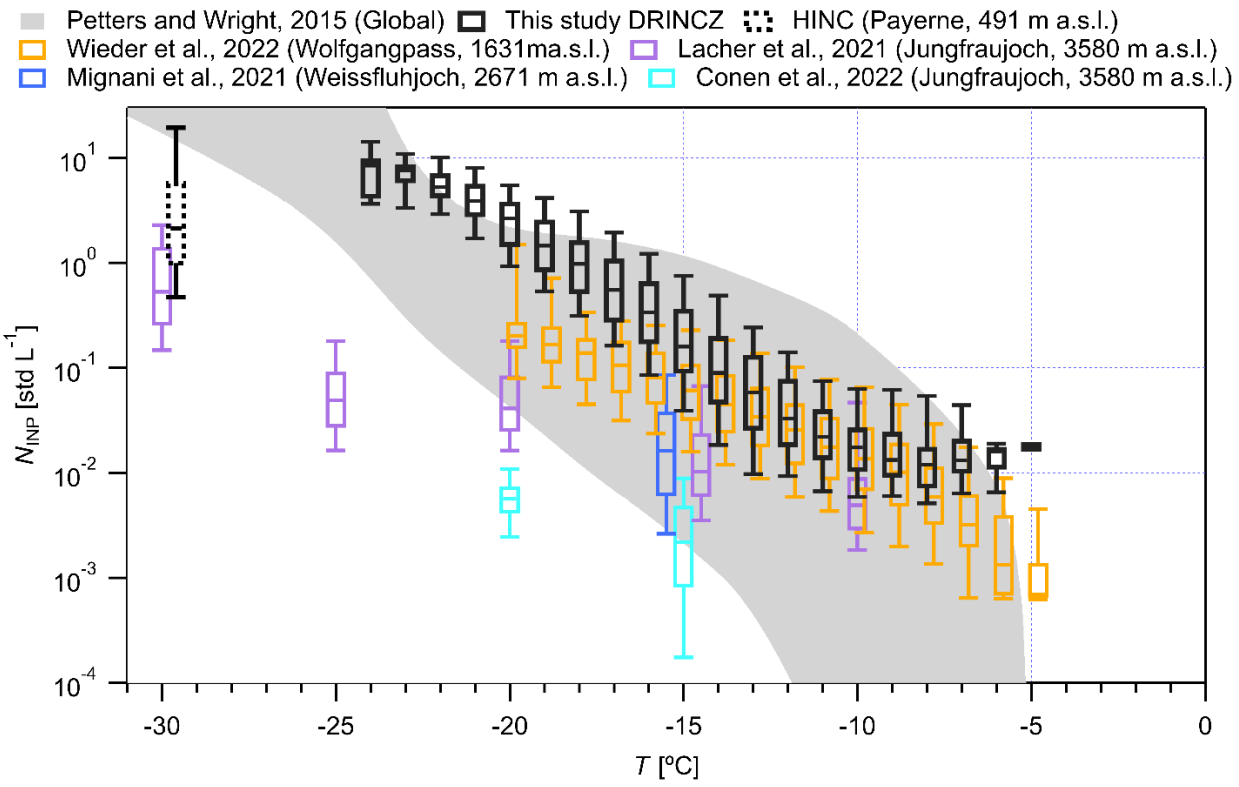

Figure S5. Comparison of PERCILES N_{INP} values against previous field studies in the Alpine region. Box plots show the N_{INP} observed in this study contrasted against an reported global envelope(Petters and Wright, 2015) and INP levels reported in selected field campaigns at different sites in the Alpine region (Wieder et al., 2022; Mignani et al., 2021; Conen et al., 2022; Lacher et al., 2021). Each box presents data points in a T interval of 1°C. The box shows the median line and the range between 25th and 75th quartiles. The lower and upper caps of the box indicate the 9th and 91th percentiles, respectively. Boxes for INPs at −15°C in Lacher et al. (2021) and Mignani et al. (2021) are offset by −0.5°C for legibility.

S8 Visual evidence on the presence of dust and biological particles

Figures S6 to S8 present microscopy images for Hirst samples collected on 20, 21 and 22 Jun 2023 during the dust period defined in Fig. 2d in the main text. In general, it shows that mineral dust particles are most abundant. It also shows the presence of different types of biological particles, including plant debris, pollen particles and spores.

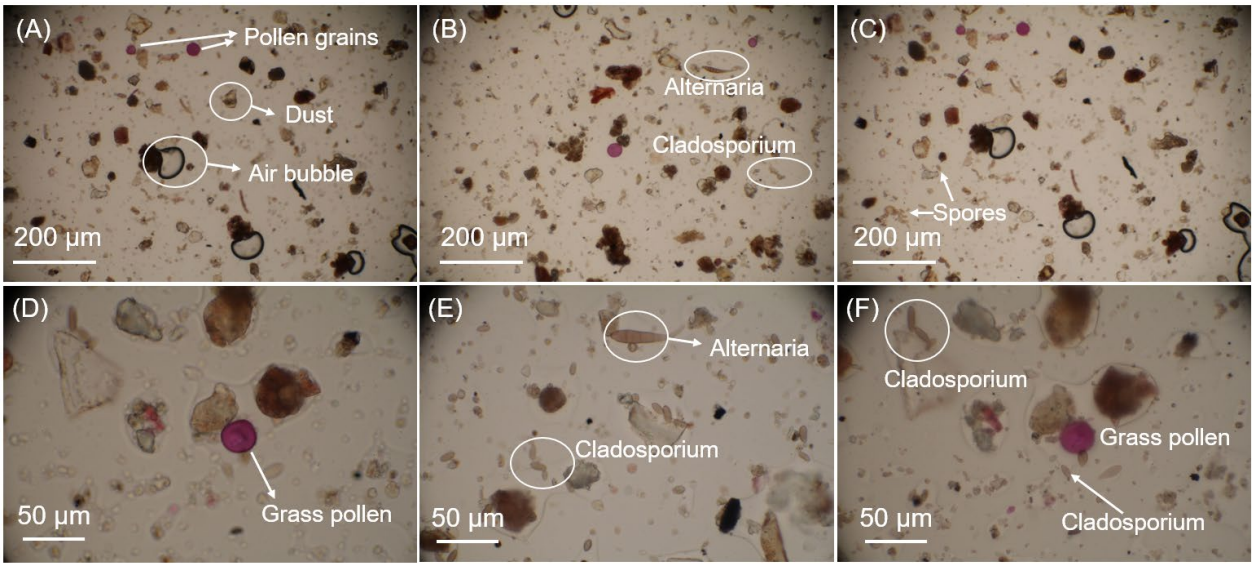

Figure S6. Microscopy images for particles from Hirst samples on 20 Jun 2023 relevant for an INP sample ID=55. Scale bars are indicated in each image. Dust particles are the most prevalent particles. Different biological particles, including pollen grains and spores, are recognized. Recognized exemplary particles are indicated in the figure.

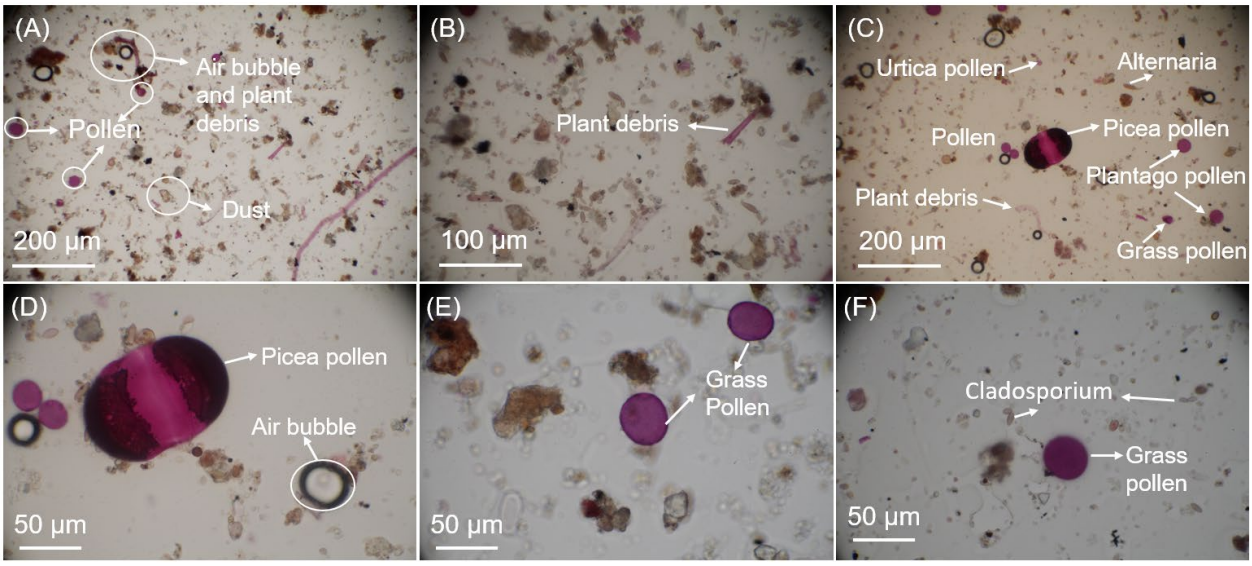

Figure S7. Microscopy images for particles from Hirst samples on 21 Jun 2023 relevant for an INP sample ID=62. Scale bars are indicated in each image. Dust particles are the most prevalent particles. Different biological particles, including pollen grains and spores, are recognized. Recognized exemplary particles are indicated in the figure.

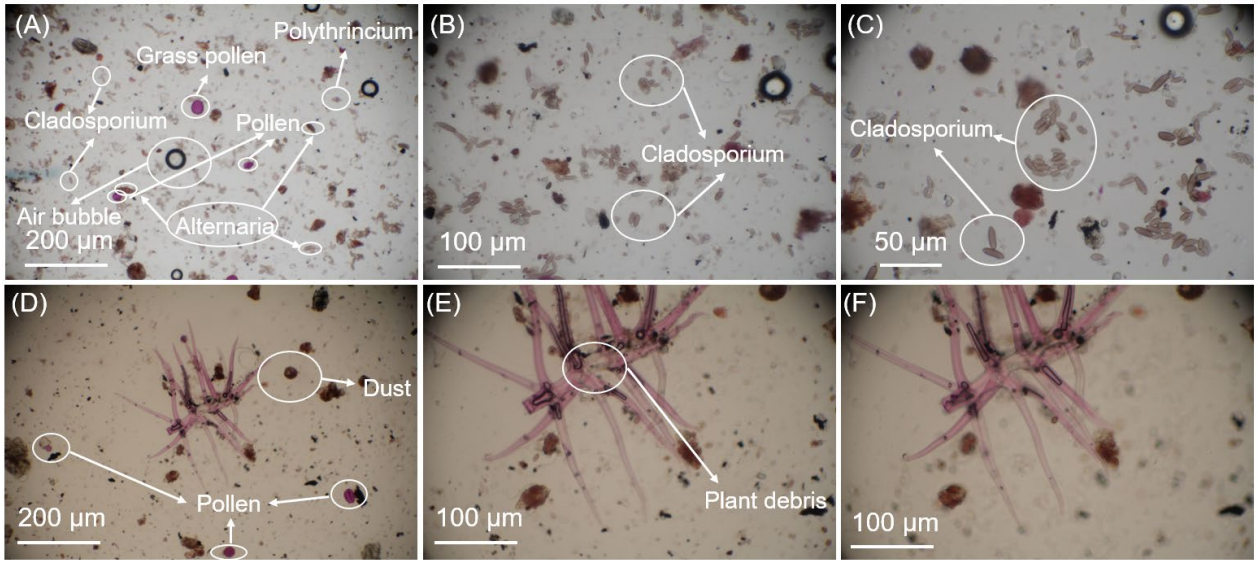

Figure S8. Microscopy images for particles from Hirst samples on 22 Jun 2023 relevant for an INP sample ID=70. Dust particles show presence in the figure. Different biological particles, including pollen grains and spores, are recognized. Recognized exemplary particles are indicated in the figure.

S9 Supplemental results for aerosol properties of each INP sample

Figure S9 provides supplemental results and data about the in-situ aerosol properties for each sample. Figure S9a shows the number concentration of total and coarse-sized particles monitored by WIBS ($Total_{WIBS}$ and $Total_{WIBS>2.5\mu m}$), as well as the number concentration of total and coarse-sized fluorescent particles ($Fluo_{WIBS}$ and $Fluo_{WIBS>2.5\mu m}$). Figure S9b compares the number concentration of coarse-sized particles represented by $\Delta Coarse_{>2.5\mu m}$ and $\Delta Coarse_{>2.5\mu m,nonFluo}$ standing for an upper and lower limit of dust particle estimation, respectively. It shows that $\Delta Coarse_{>2.5\mu m}$ and $\Delta Coarse_{>2.5\mu m,nonFluo}$ are strongly and significantly correlated, showing a Pearson coefficient $\rho_{Pearson}$=0.97 (p=2.58E−51). The difference between $\Delta Coarse_{>2.5\mu m}$ and $\Delta Coarse_{>2.5\mu m,nonFluo}$ are generally smaller than 10%, suggesting that they can substitute for each other during dust period. The larger difference between $\Delta Coarse_{>2.5\mu m}$ and $\Delta Coarse_{>2.5\mu m,nonFluo}$ for samples with ID numbers between 76 and 81 may be due to the dual effects of precipitation (Fig. 2f). It results from an increase in ABC_{WIBS} due to enhanced bioaerosol release but also a wet removal of other aerosol particles (Gao et al., 2024). Figure S9d shows that PM10 and PM2.5 values are generally higher for samples during the defined dust period in comparison to other samples. Figure S9e provides the ambient temperature ($T_{Ambient}$) and relative humidity with respect to water (RH_w) for INP samples. Both $T_{Ambient}$ and RH_w are the average of data points monitored over the course of sampling. The $T_{Ambient}$ ranges between 30 and −5°C, implying a large spread of bioaerosols emission rates across different seasons (Schneider et al., 2021).

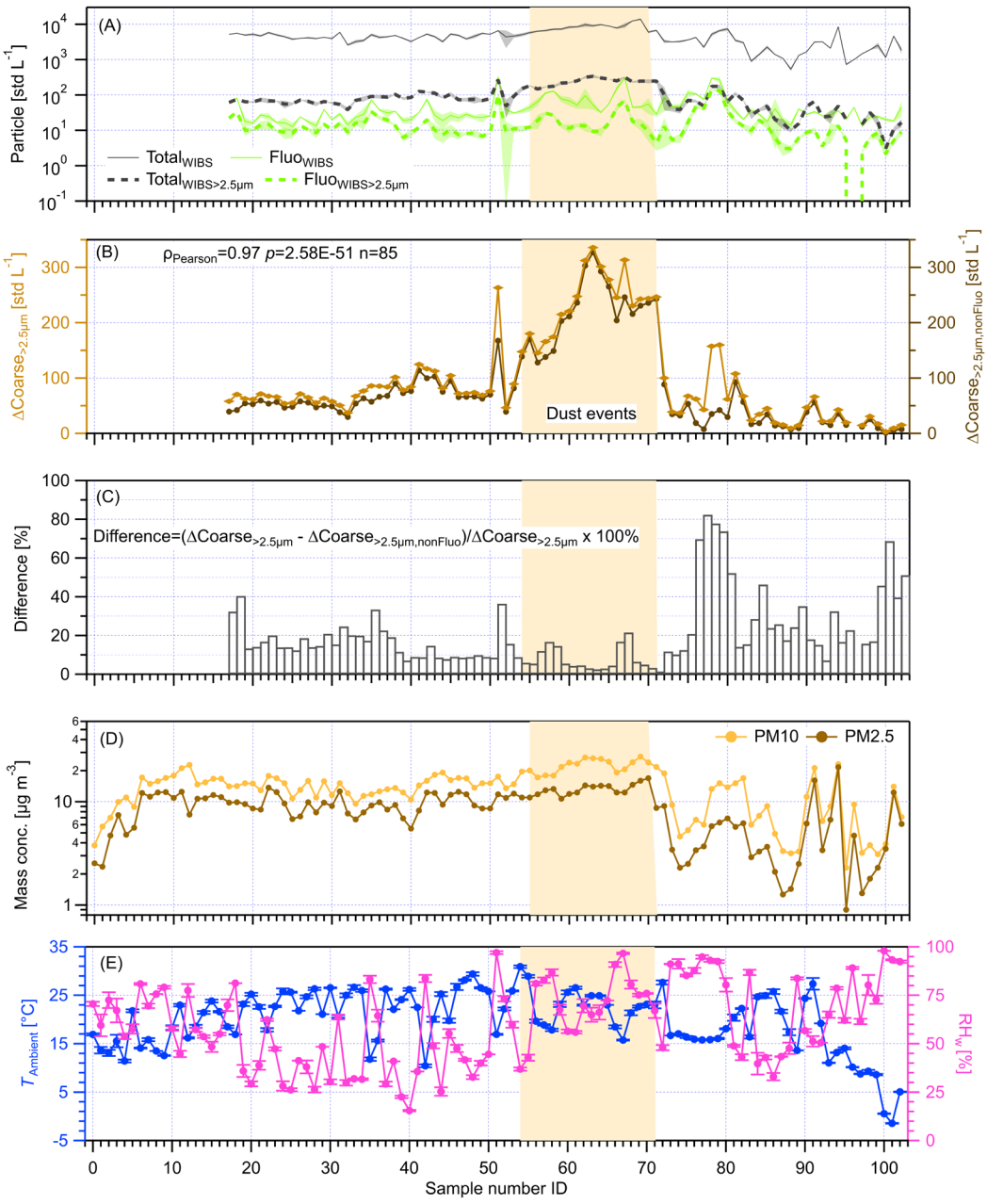

Figure S9. Overview of different aerosol properties for all IN samples. (a) The number concentration of total particles (Total$_{WIBS}$) and fluorescent particles (Fluo$_{WIBS}$) monitored by WIBS, and corresponding coarse-sized particle (Total$_{WIBS>2.5µm}$ and Fluo$_{WIBS>2.5µm}$). (b) The number concentration of coarse-sized particles represented by ΔCoarse$_{>2.5µm}$ and ΔCoarse$_{>2.5µm,nonFluo}$ standing for an upper and lower limit of dust particle estimation, respectively. ΔCoarse$_{>2.5µm}$ is the number concentration difference between Total$_{WIBS>2.5µm}$ and ABC$_{WIBS>2.5µm}$, and ΔCoarse$_{>2.5µm,nonFluo}$ is the number concentration difference between Total$_{WIBS>2.5µm}$ and Fluo$_{WIBS>2.5µm}$. (c) Comparison of ΔCoarse$_{>2.5µm}$ and ΔCoarse$_{>2.5µm,nonFluo}$.

(d) PM10 and PM2.5. (e) $T_{Ambient}$ and RH_w. The error bar indicates the standard deviation calculated for data points within the sampling time.

S10 Precipitation effects on aerosol properties and INP abundance

Three groups of samples before and during precipitation (time gap <4 hours, see Table S1) were collected between 21 and 23 June 2023 (Fig. S10), to investigate the immediate effect of precipitation events on aerosol properties and INP abundance. Figure S10a shows that precipitation leads to pronounced INP decreases for Group 1 for $-22< T <-11$°C by up to ~88% (~ −15°C), whereas it shows insignificant influence on INPs at other *T*s. The precipitation event decreases ABC_{WIBS} from 3.3 to 2.2 std L^{-1} (Fig. S10b), suggesting a particle wash-out effect (Gao et al., 2024; Prenni et al., 2013), which may explain the decreased INPs (Coluzza et al., 2017). The slightly increased $ABC_{WIBS>2.5\mu m}$ (by 0.02 std L^{-1} in Fig. S10b) suggests that decreased ABC_{WIBS} is attributed to the decrease in $ABC_{WIBS<2.5\mu m}$. This means decreased $ABC_{WIBS<2.5\mu m}$ caused by precipitation removal is responsible for INP decreases of the sample for $-18< T <-13$°C. In addition, the precipitation event does not show pronounced effects on INPs observed for Group 2 (Fig. S10c), consistent with its small changes in ABC_{WIBS} (2% increase) and $ABC_{WIBS<2.5\mu m}$ (−10% decrease). Group 3 shows slightly decreased INPs for $T>-18$°C during precipitation (Fig. S10e), which may be associated with decreases in $ABC_{WIBS<2.5\mu m}$ by 0.39 std L^{-1} (−60% in Fig. S10f), despite with increased ABC_{WIBS} (by ~17%) and $ABC_{WIBS>2.5\mu m}$ (by ~28%) particles (e.g., pollen) which may be not effective particle for warm *T*s (Fig. 4).

Figure S10 generally shows that precipitation has wash-out effects (Gao et al., 2024) on aerosol particles and INPs, showing decreased $ABC_{WIBS<2.5\mu m}$ particles (Fig. S10b, d and e, e.g., soil dust and fungal spores (Gao et al., 2024)). The effect is more pronounced with short and intensive precipitation (ref. Group 1 and Fig. S11). B contrast, precipitation increases $ABC_{WIBS>2.5\mu m}$ particles across all three groups (particularly Group 3). Such an increase is possibly associated with increased $Hirst_{Total}$ pollen particles (Fig. S11) driven by raindrop splash (Huffman et al., 2013; Prenni et al., 2013), which may outweigh particle wash-out. The INP abundance change (decrease) at warm *T*s (>−18°C) is likely more driven by the wash-out effect while raindrop splash generated pollen and dust particles may contribute to INPs at lower *T*s.

Figure S11 presents high time resolution aerosol properties, including $Hirst_{Total}$, $Total_{WIBS}$, $Fluo_{WIBS}$, ABC_{WIBS}, PM10, PM2.5, TC and eBC, relevant for INP samples influenced by precipitation events and shows the corresponding meteorological data, including wind speed and direction, temperature and relative humidity with respect to water, as well as 10-min precipitation intensity. Figure S11a shows that a short but intense precipitation on 21 Jun 2023 enriches the pollen concentration by 0.47 std L^{-1} (by 134%) whereas the precipitation event on 22 Jun 2023 in the afternoon (around 5:00 PM) shows a considerable reduction in pollen particles. The pollen production for the former may be because of the intense rainfall which causes splashes on plants and thus leads to release of pollen particles (Prenni et al., 2013; Huffman et al., 2013). However, the latter case experienced strong winds which promotes the dilution and spreading of pollen particles, and thus the latter shows a sharp reduction in pollen particles. The results in Fig. S11b to d for aerosol properties generally exhibit wash-out effects of the precipitation, indicated by the decreases in the properties.

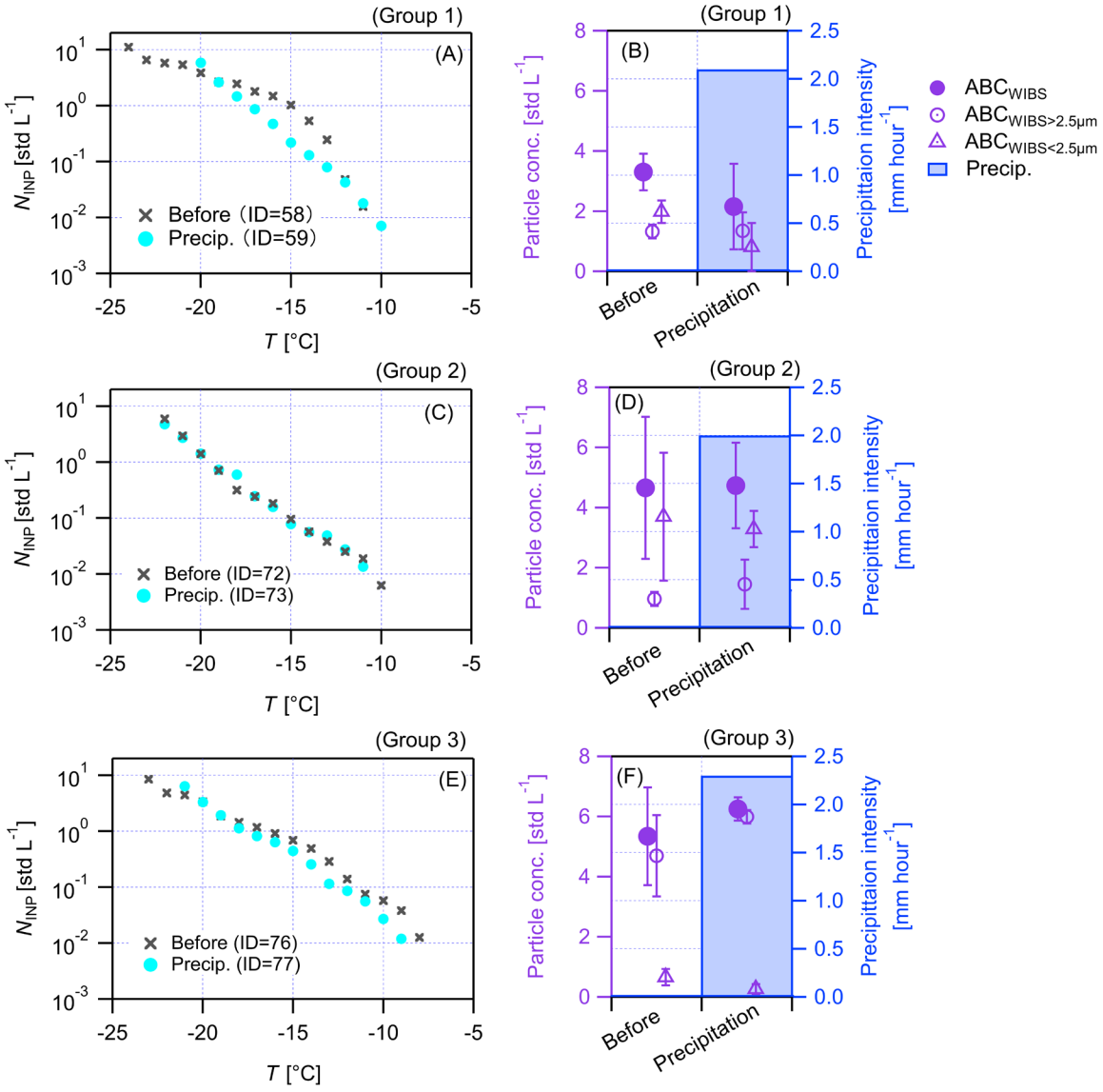

Figure S10. The precipitation effects on INP abundance and aerosol properties. Presented results include N_{INP} values at different temperatures, the concentration of ABC$_{WIBS}$, ABC$_{WIBS>2.5\mu m}$ and ABC$_{WIBS<2.5\mu m}$ (ABC$_{WIBS}$ particles smaller than 2.5µm), as well as the precipitation intensity, of samples before and during a precipitation event. Three groups of samples are presented. Panel (a) and (b) for Group 1 on 21 June 2023. Panel (c) and (d) for Group 2 on 22 June 2023. Panel (e) and (f) for Group 3 on 23 June 2023. N_{INP} values are weighted averages of at least three measurements per sample, calculated following Wieder et al. (2022)

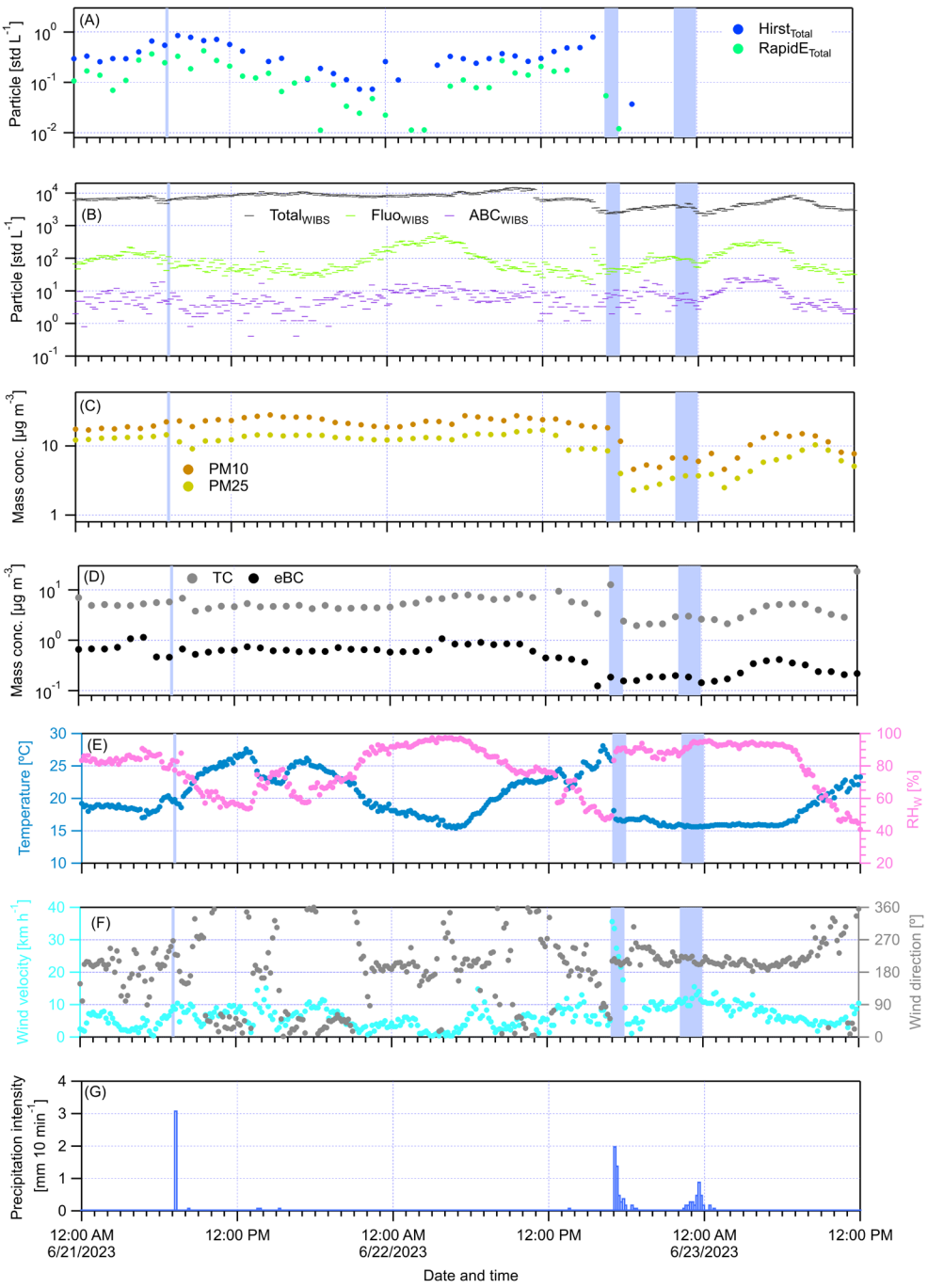

Figure S11. Timeseries of different aerosol properties for periods with and without precipitation. (a) The number concentration of RapidE$_{Total}$ and Hirst$_{Total}$ particles. (b) The number concentration difference between Total$_{WIBS}$, Fluo$_{WIBS}$ and ABC$_{WIBS}$ particles. (c) The mass concentration of PM10 and PM2.5. (d) The mass concentration of TC and eBC. (e) The ambient temperature (on the left axis) and relative humidity (RH$_w$, on the right axis). (f) Horizontal wind velocity (on the left axis) and wind direction (on the right axis). (g) The precipitation intensity for the period of IN sampling. All concentration values were corrected

to equivalent atmospheric standard condition (i.e., per standard volume of sampled air, std). The shading areas indicates different precipitation periods.

S11 Supplemental results for INP source apportionment of different samples

Figures S12 to S19 provide results for INP source apportionment for more INP samples, in addition to the case study presented in Fig. 3 in the main text. The results generally show that both FBAPs and coarse-sized dust particles may be relevant INPs. Biomass burning particles are also present and may influence the INP abundance of different samples. The implications from these figures are qualitative results and can enlighten further analysis investigating the single role of each INP source.

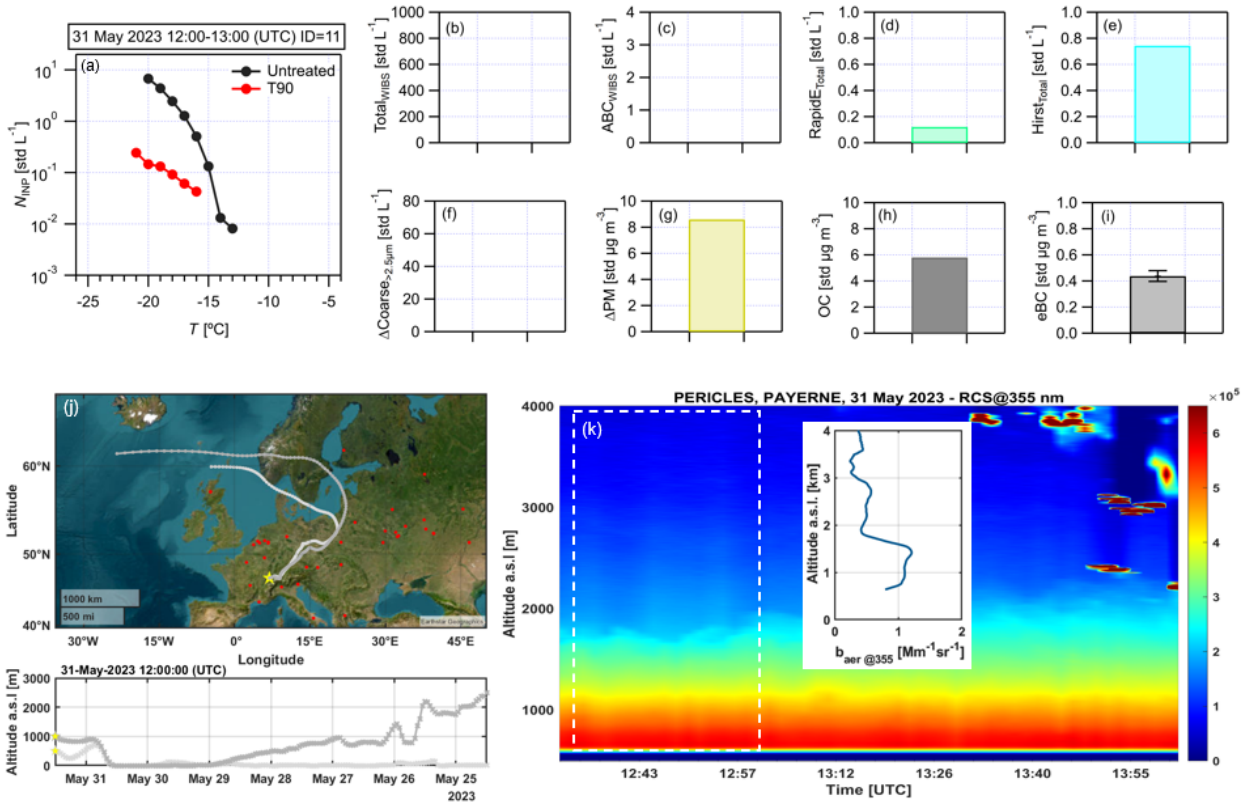

Figure S12. Aerosol properties from in situ, modelling and remote sensing measurements during the INP sampling period for a sample (ID=11) collected on 31 May 2023, between 22:00 and 22:30 (UTC). (a) The INP number concentrations (N_{INP}) of untreated and 90°C heated (T90) samples. (b) Total$_{WIBS}$ particle number concentration. (c) ABC$_{WIBS}$ particle number concentration. (d) RapidE$_{Total}$ particle number concentration. (e) Hirst$_{Total}$ particle number concentration. (f) ΔCoarse$_{>2.5μm}$ particle number concentration. (g) ΔPM mass concentration. (h) Organic carbon (OC) mass concentration. (i) Elemental black carbon (eBC) mass concentration. (j) Airmass atmospheric trajectories at 500 and 1000 m a.g.l. acquired by Hybrid Single–Particle Lagrangian Integrated Trajectory (HYSPLIT). The red dots indicate fire spots in the last 7 days. (k) Spatio-temporal evolution of the aerosol range-corrected lidar signals using the analogue detection mode at 355 nm (RCS@355nm), with inset the averaged vertical profile of the aerosol backscatter coefficient at 355 nm (b$_{aer@355}$) for the period of INP sampling (time window indicated by the white dashed square). The error bars for bar plots represent 1 standard deviation of corresponding measurements. N_{INP} values are weighted averages of at least three measurements per sample, calculated following Wieder et al. (2022).

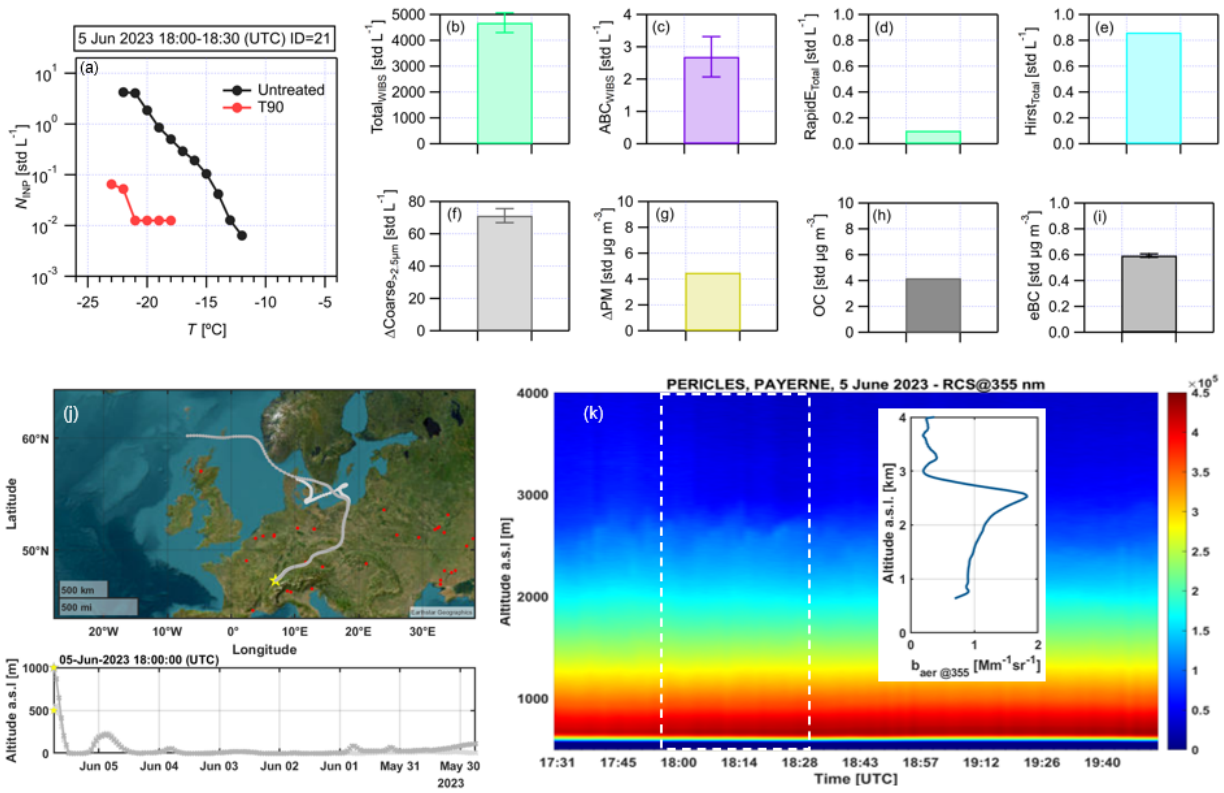

Figure S13. Aerosol properties from in situ, modelling and remote sensing measurements during the INP sampling period for a sample (ID=21) collected on 5 Jun 2023, between 22:00 and 22:30 (UTC). (a) The INP number concentrations (N_{INP}) of untreated and 90°C heated (T90) samples. (b) $Total_{WIBS}$ particle number concentration. (c) ABC_{WIBS} particle number concentration. (d) $RapidE_{Total}$ particle number concentration. (e) $Hirst_{Total}$ particle number concentration. (f) $\Delta Coarse_{>2.5\mu m}$ particle number concentration. (g) ΔPM mass concentration. (h) Organic carbon (OC) mass concentration. (i) Elemental black carbon (eBC) mass concentration. (j) Airmass atmospheric trajectories at 500 and 1000 m a.g.l. acquired by Hybrid Single–Particle Lagrangian Integrated Trajectory (HYSPLIT). The red dots indicate fire spots in the last 7 days. (k) Spatio-temporal evolution of the aerosol range-corrected lidar signals using the analogue detection mode at 355 nm (RCS@355nm), with inset the averaged vertical profile of the aerosol backscatter coefficient at 355 nm ($b_{aer@355}$) for the period of INP sampling (time window indicated by the white dashed square). The error bars for bar plots represent 1 standard deviation of corresponding measurements. N_{INP} values are weighted averages of at least three measurements per sample, calculated following Wieder et al. (2022).

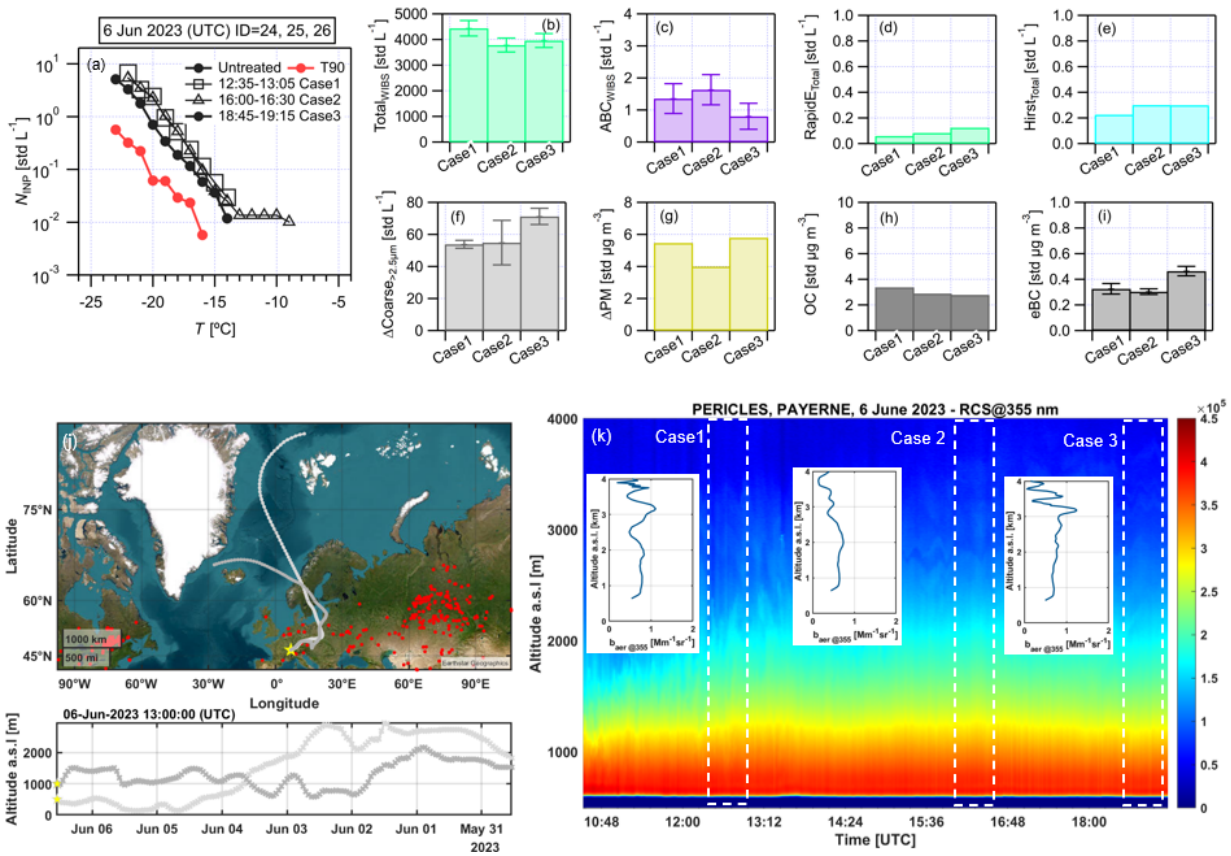

Figure S14. Aerosol properties from in situ, modelling and remote sensing measurements during the INP sampling period for three samples (ID=24, 25 and 26) collected on 6 Jun 2023, between 22:00 and 22:30 (UTC). (a) The INP number concentrations (N_{INP}) of untreated and 90°C heated (T90) samples. (b) Total$_{WIBS}$ particle number concentration. (c) ABC$_{WIBS}$ particle number concentration. (d) RapidE$_{Total}$ particle number concentration. (e) Hirst$_{Total}$ particle number concentration. (f) ΔCoarse$_{>2.5μm}$ particle number concentration. (g) ΔPM mass concentration. (h) Organic carbon (OC) mass concentration. (i) Elemental black carbon (eBC) mass concentration. (j) Airmass atmospheric trajectories at 500 and 1000 m a.g.l. acquired by Hybrid Single–Particle Lagrangian Integrated Trajectory (HYSPLIT). The red dots indicate fire spots in the last 7 days. (k) Spatio-temporal evolution of the aerosol range-corrected lidar signals using the analogue detection mode at 355 nm (RCS@355nm), with inset the averaged vertical profile of the aerosol backscatter coefficient at 355 nm ($b_{aer@355}$) for the period of INP sampling (time window indicated by the white dashed square). The error bars for bar plots represent 1 standard deviation of corresponding measurements. N_{INP} values are weighted averages of at least three measurements per sample, calculated following Wieder et al. (2022).

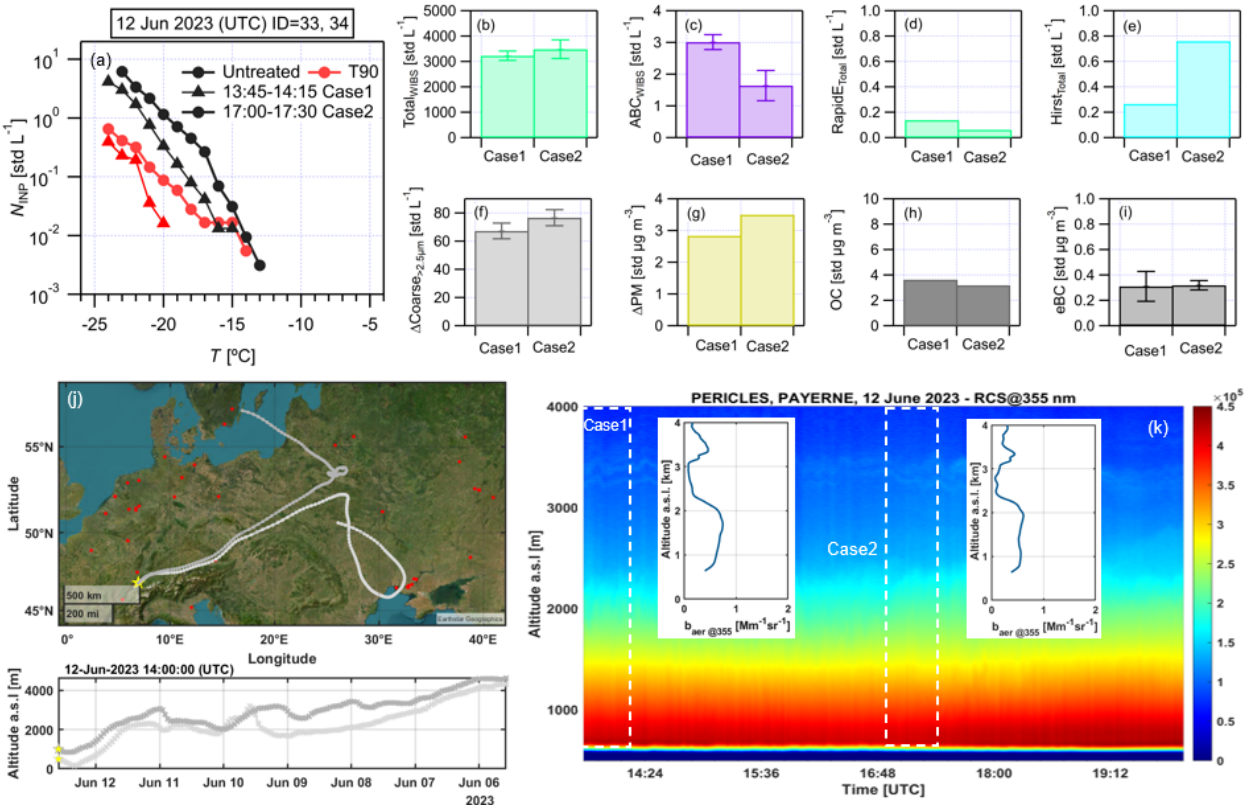

Figure S15. Aerosol properties from in situ, modelling and remote sensing measurements during the INP sampling period for two samples (ID=33 and 34) collected on 12 Jun 2023, between 22:00 and 22:30 (UTC). (a) The INP number concentrations (N_{INP}) of untreated and 90°C heated (T90) samples. (b) $Total_{WIBS}$ particle number concentration. (c) ABC_{WIBS} particle number concentration. (d) $RapidE_{Total}$ particle number concentration. (e) $Hirst_{Total}$ particle number concentration. (f) $\Delta Coarse_{>2.5\mu m}$ particle number concentration. (g) ΔPM mass concentration. (h) Organic carbon (OC) mass concentration. (i) Elemental black carbon (eBC) mass concentration. (j) Airmass atmospheric trajectories at 500 and 1000 m a.g.l. acquired by Hybrid Single–Particle Lagrangian Integrated Trajectory (HYSPLIT). The red dots indicate fire spots in the last 7 days. (k) Spatio-temporal evolution of the aerosol range-corrected lidar signals using the analogue detection mode at 355 nm (RCS@355nm), with inset the averaged vertical profile of the aerosol backscatter coefficient at 355 nm ($b_{aer@355}$) for the period of INP sampling (time window indicated by the white dashed square). The error bars for bar plots represent 1 standard deviation of corresponding measurements. N_{INP} values are weighted averages of at least three measurements per sample, calculated following Wieder et al. (2022).

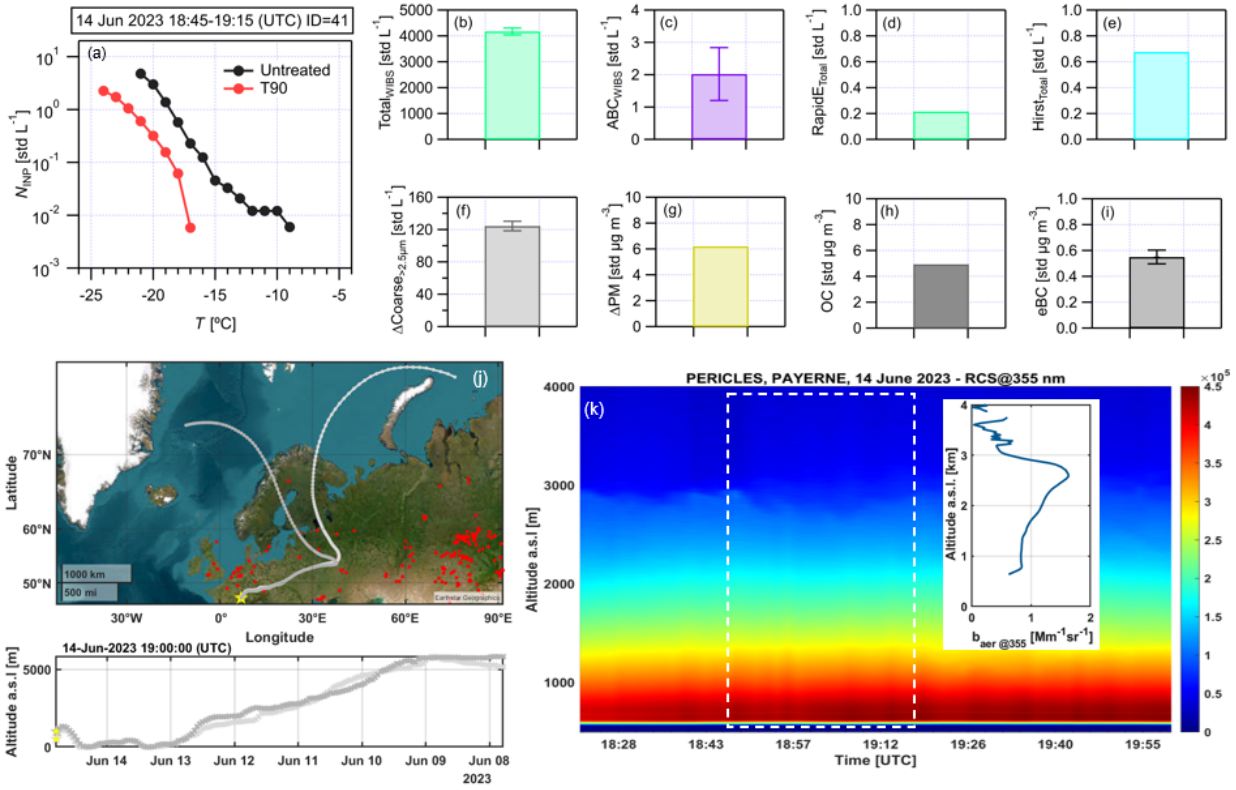

Figure S16. Aerosol properties from in situ, modelling and remote sensing measurements during the INP sampling period for a sample (ID=41) collected on 14 Jun 2023, between 22:00 and 22:30 (UTC). (a) The INP number concentrations (N_{INP}) of untreated and 90°C heated (T90) samples. (b) Total$_{WIBS}$ particle number concentration. (c) ABC$_{WIBS}$ particle number concentration. (d) RapidE$_{Total}$ particle number concentration. (e) Hirst$_{Total}$ particle number concentration. (f) ΔCoarse$_{>2.5μm}$ particle number concentration. (g) ΔPM mass concentration. (h) Organic carbon (OC) mass concentration. (i) Elemental black carbon (eBC) mass concentration. (j) Airmass atmospheric trajectories at 500 and 1000 m a.g.l. acquired by Hybrid Single–Particle Lagrangian Integrated Trajectory (HYSPLIT). The red dots indicate fire spots in the last 7 days. (k) Spatio-temporal evolution of the aerosol range-corrected lidar signals using the analogue detection mode at 355 nm (RCS@355nm), with inset the averaged vertical profile of the aerosol backscatter coefficient at 355 nm (b$_{aer@355}$) for the period of INP sampling (time window indicated by the white dashed square). The error bars for bar plots represent 1 standard deviation of corresponding measurements. N_{INP} values are weighted averages of at least three measurements per sample, calculated following Wieder et al. (2022).

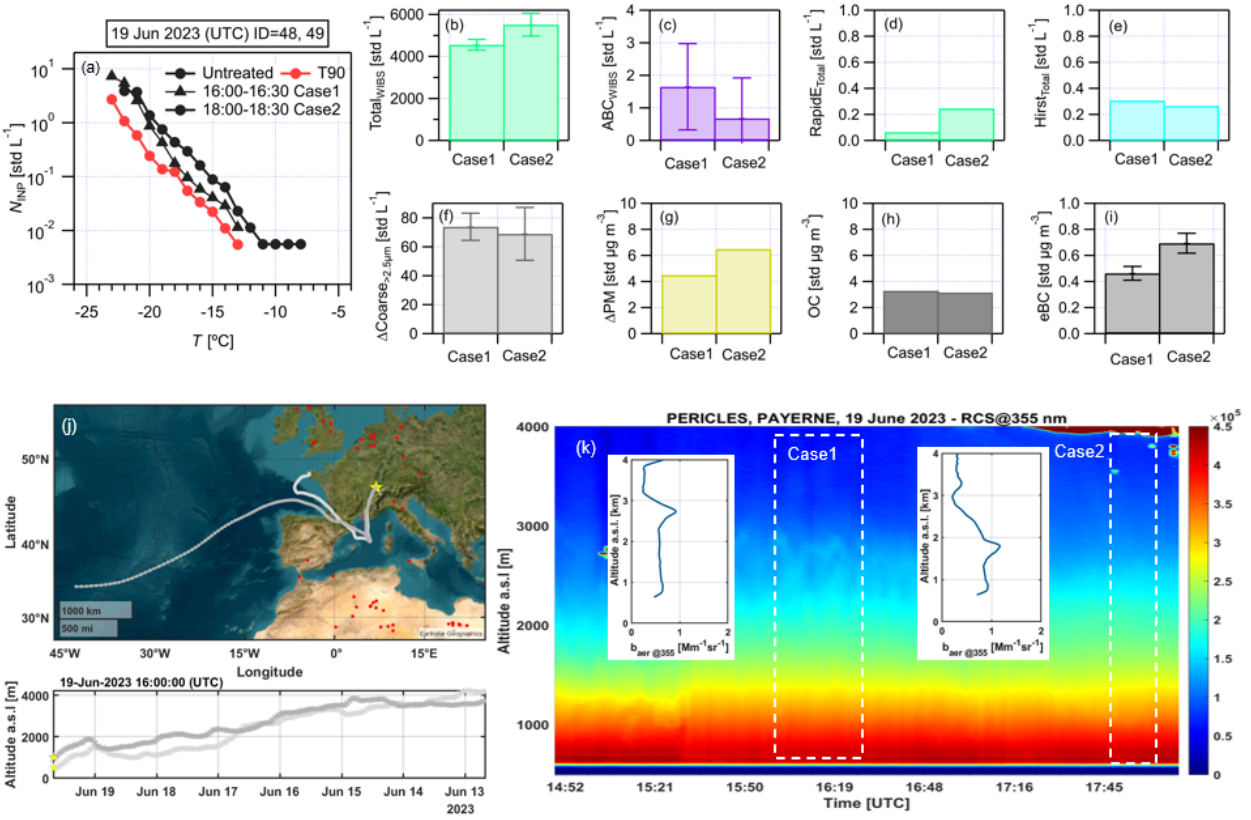

Figure S17. Aerosol properties from in situ, modelling and remote sensing measurements during the INP sampling period for two samples (ID= 48 and 49) collected on 19 Jun 2023, between 22:00 and 22:30 (UTC). (a) The INP number concentrations (N_{INP}) of untreated and 90°C heated (T90) samples. (b) Total$_{WIBS}$ particle number concentration. (c) ABC$_{WIBS}$ particle number concentration. (d) RapidE$_{Total}$ particle number concentration. (e) Hirst$_{Total}$ particle number concentration. (f) ΔCoarse$_{>2.5μm}$ particle number concentration. (g) ΔPM mass concentration. (h) Organic carbon (OC) mass concentration. (i) Elemental black carbon (eBC) mass concentration. (j) Airmass atmospheric trajectories at 500 and 1000 m a.g.l. acquired by Hybrid Single–Particle Lagrangian Integrated Trajectory (HYSPLIT). The red dots indicate fire spots in the last 7 days. (k) Spatio-temporal evolution of the aerosol range-corrected lidar signals using the analogue detection mode at 355 nm (RCS@355nm), with inset the averaged vertical profile of the aerosol backscatter coefficient at 355 nm ($b_{aer@355}$) for the period of INP sampling (time window indicated by the white dashed square). The error bars for bar plots represent 1 standard deviation of corresponding measurements. N_{INP} values are weighted averages of at least three measurements per sample, calculated following Wieder et al. (2022).

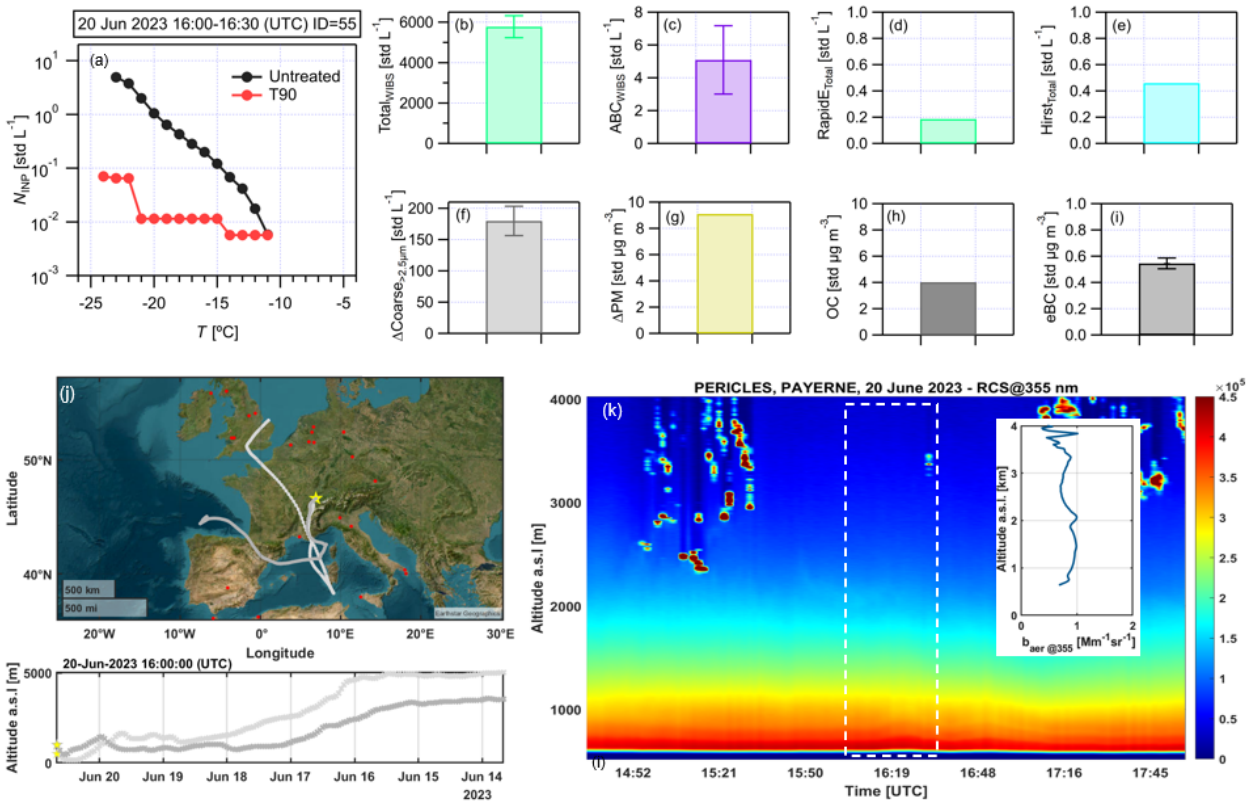

Figure S18. Aerosol properties from in situ, modelling and remote sensing measurements during the INP sampling period for a sample (ID=55) collected on 20 Jun 2023, between 22:00 and 22:30 (UTC). (a) The INP number concentrations (N_{INP}) of untreated and 90°C heated (T90) samples. (b) $Total_{WIBS}$ particle number concentration. (c) ABC_{WIBS} particle number concentration. (d) $RapidE_{Total}$ particle number concentration. (e) $Hirst_{Total}$ particle number concentration. (f) $\Delta Coarse_{>2.5\mu m}$ particle number concentration. (g) ΔPM mass concentration. (h) Organic carbon (OC) mass concentration. (i) Elemental black carbon (eBC) mass concentration. (j) Airmass atmospheric trajectories at 500 and 1000 m a.g.l. acquired by Hybrid Single–Particle Lagrangian Integrated Trajectory (HYSPLIT). The red dots indicate fire spots in the last 7 days. (k) Spatio-temporal evolution of the aerosol range-corrected lidar signals using the analogue detection mode at 355 nm (RCS@355nm), with inset the averaged vertical profile of the aerosol backscatter coefficient at 355 nm ($b_{aer@355}$) for the period of INP sampling (time window indicated by the white dashed square). The error bars for bar plots represent 1 standard deviation of corresponding measurements. N_{INP} values are weighted averages of at least three measurements per sample, calculated following Wieder et al. (2022).

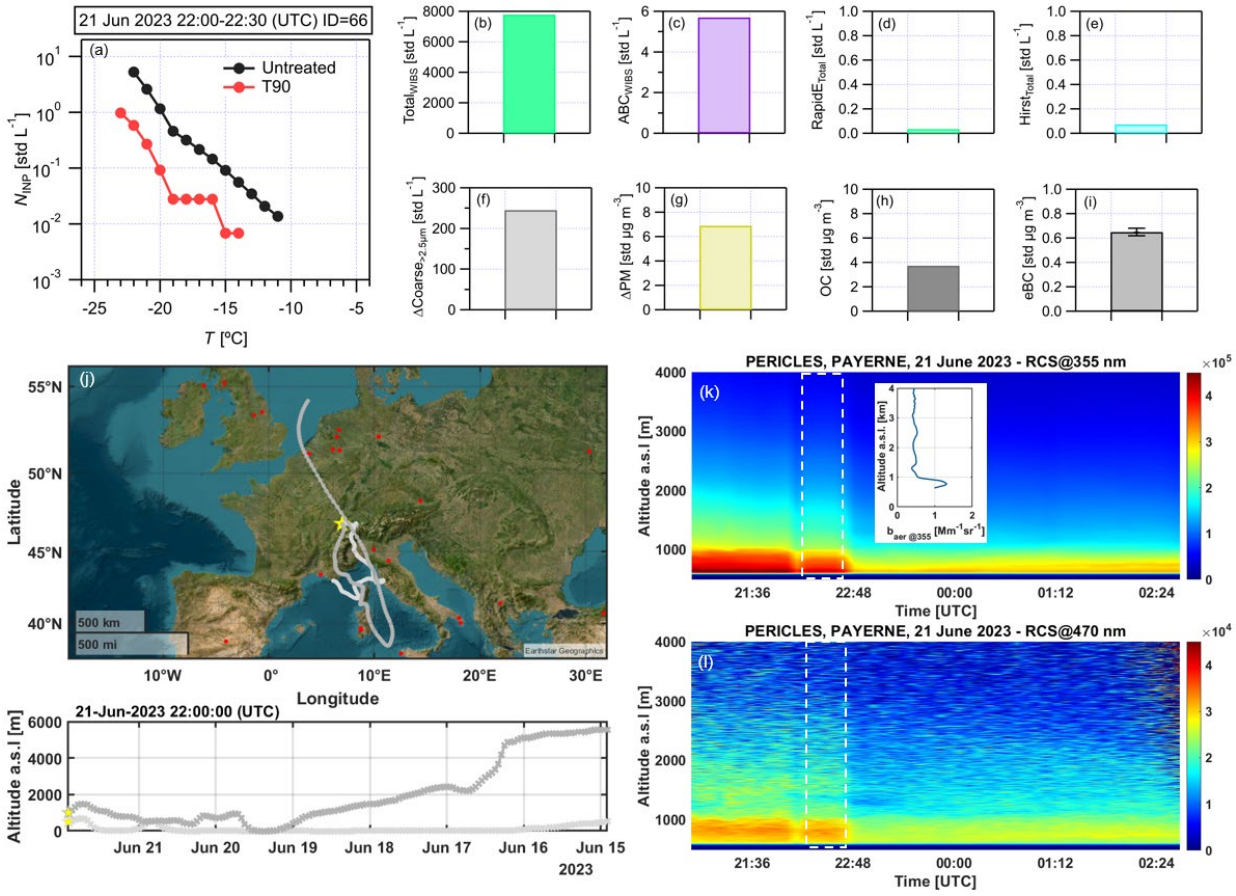

Figure S19. Aerosol properties from in situ, modelling and remote sensing measurements during the INP sampling period for a sample (ID=66) collected on 21 Jun 2023, between 22:00 and 22:30 (UTC). (a) The INP number concentrations (N_{INP}) of untreated and 90°C heated (T90) samples. (b) Total$_{WIBS}$ particle number concentration. (c) ABC$_{WIBS}$ particle number concentration. (d) RapidE$_{Total}$ particle number concentration. (e) Hirst$_{Total}$ particle number concentration. (f) ΔCoarse$_{>2.5μm}$ particle number concentration. (g) ΔPM mass concentration. (h) Organic carbon (OC) mass concentration. (i) Elemental black carbon (eBC) mass concentration. (j) Airmass atmospheric trajectories at 500 and 1000 m a.g.l. acquired by Hybrid Single–Particle Lagrangian Integrated Trajectory (HYSPLIT). The red dots indicate fire spots in the last 7 days. (k) Spatio-temporal evolution of the aerosol range-corrected lidar signals using the analogue detection mode at 355 nm (RCS@355nm), with inset the averaged vertical profile of the aerosol backscatter coefficient at 355 nm (b$_{aer@355}$) for the period of INP sampling (time window indicated by the white dashed square). The error bars for bar plots represent 1 standard deviation of corresponding measurements. N_{INP} values are weighted averages of at least three measurements per sample, calculated following Wieder et al. (2022).

S12 Detailed statistical analysis for correlations between N_{INP} and different aerosol properties

Figures S20 to S29 provide detailed statistical analysis for the correlations between N_{INP} and different aerosol properties. Each figure shows the scatter plots of N_{INP} values at different temperatures and different aerosol properties, including $Total_{WIBS}$, $Fluo_{WIBS}$, ABC_{WIBS}, $ABC_{WIBS>2.5\mu m}$, $Hirst_{Total}$, $RapidE_{Total}$, $\Delta Coarse_{>2.5\mu m}$, ΔPM, OC and eBC. The calculated Pearson and Spearman coefficients ($\rho_{Pearson}$ and $\rho_{Spearman}$) values and corresponding p values, as well as the number of data points (n) are also indicated in the figure. Significant correlations ($p<0.05$) are marked in red in the figure. Additionally, we note that the numbers of data points for the case of T=−5°C and −24°C are less than 10 in Figs. S20 to S29. Thus, the corresponding results (also in Fig. 4) are of a lower confidence level compared to the results at other temperatures.

The results presented in Figs. S20 to S29 support the discussions in the main text to evaluate the contribution of different aerosols to INPs. As demonstrated in the main text, FBAPs represented by ABC_{WIBS} and $ABC_{WIBS>2.5\mu m}$, make significant contributions to the observed INPs for $T \geq -20$°C. The scatter plots of ABC_{WIBS} and N_{INP} at −20°C (Fig. S22o) show that approximately 99% of N_{INP} and ABC_{WIBS} values are within a factor of 10. Similarly, Fig. S21n (Fig. S23o) shows that 99% of $ABC_{WIBS>2.5\mu m}$ observations stay a range of two orders of magnitude compared to N_{INP} values at −19°C (−20°C). Such compact data distributions also suggest both ABC_{WIBS} and $ABC_{WIBS>2.5\mu m}$ particles are important and significant contributors to the observed INPs for $T \geq -20$°C. Also, statistical analysis in the main text demonstrated that PBAPs represented by $Hirst_{Total}$ pollen particles significantly contributed to the observed INPs for T between −16°C and −21°C (Fig. 4 in the main text), which is also shown in Fig. S22. The scatter plots in Fig. S24o show that 69% of $Hirst_{Total}$ observations stay a range of two orders of magnitude compared to at N_{INP} values at −20°C, which is smaller than that of ABC_{WIBS} and $ABC_{WIBS>2.5\mu m}$. This means pollen particles detected by Hirst contribute only a fraction of INPs at −20°C. In other words, ABC_{WIBS} and $ABC_{WIBS>2.5\mu m}$ may include more types of INPs at −20°C, including large-sized pollen, and small-sized spores, bacteria agglomerates. Additionally, we note that $RapidE_{Total}$ may be a lower estimation of INPs at −20°C (also −21°C) contributed by pollens compared to the case of $Hirst_{Total}$, as shown significant correlations with the N_{INP} values but shown a small fraction (0.23, 0.05 for T=−21°C) of data points within a factor of 10 (Fig. S25o and p). Also, wo note that RapidE is still an instrument under development and no metrological validation of the instrument has been performed yet.

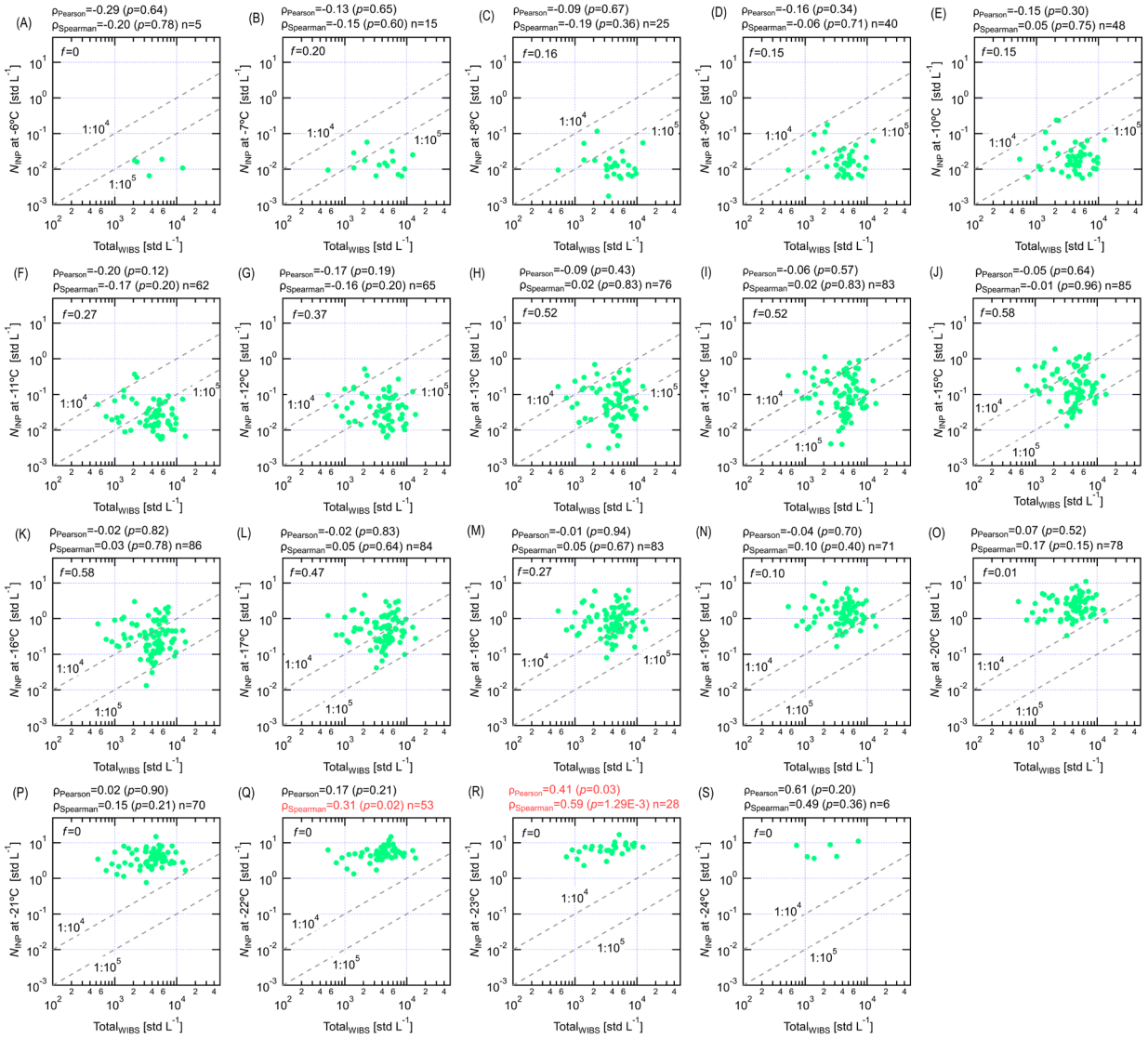

Figure S20. The correlation coefficients ($\rho_{Pearson}$ and $\rho_{Spearman}$) between INP number concentrations at a fixed *T* (on the *x*-axis) for untreated samples and $Total_{WIBS}$ particle number concentration. Panels (a) to (s) are for INP number concentrations tested from −6 to −24°C. Both $\rho_{Pearson}$ and $\rho_{Spearman}$ coefficients and corresponding *p* values are provided at the top of each panel. Significant correlations ($p<0.05$) are indicated in red. The *f* value means the fraction of data points within the range specified in the figure.

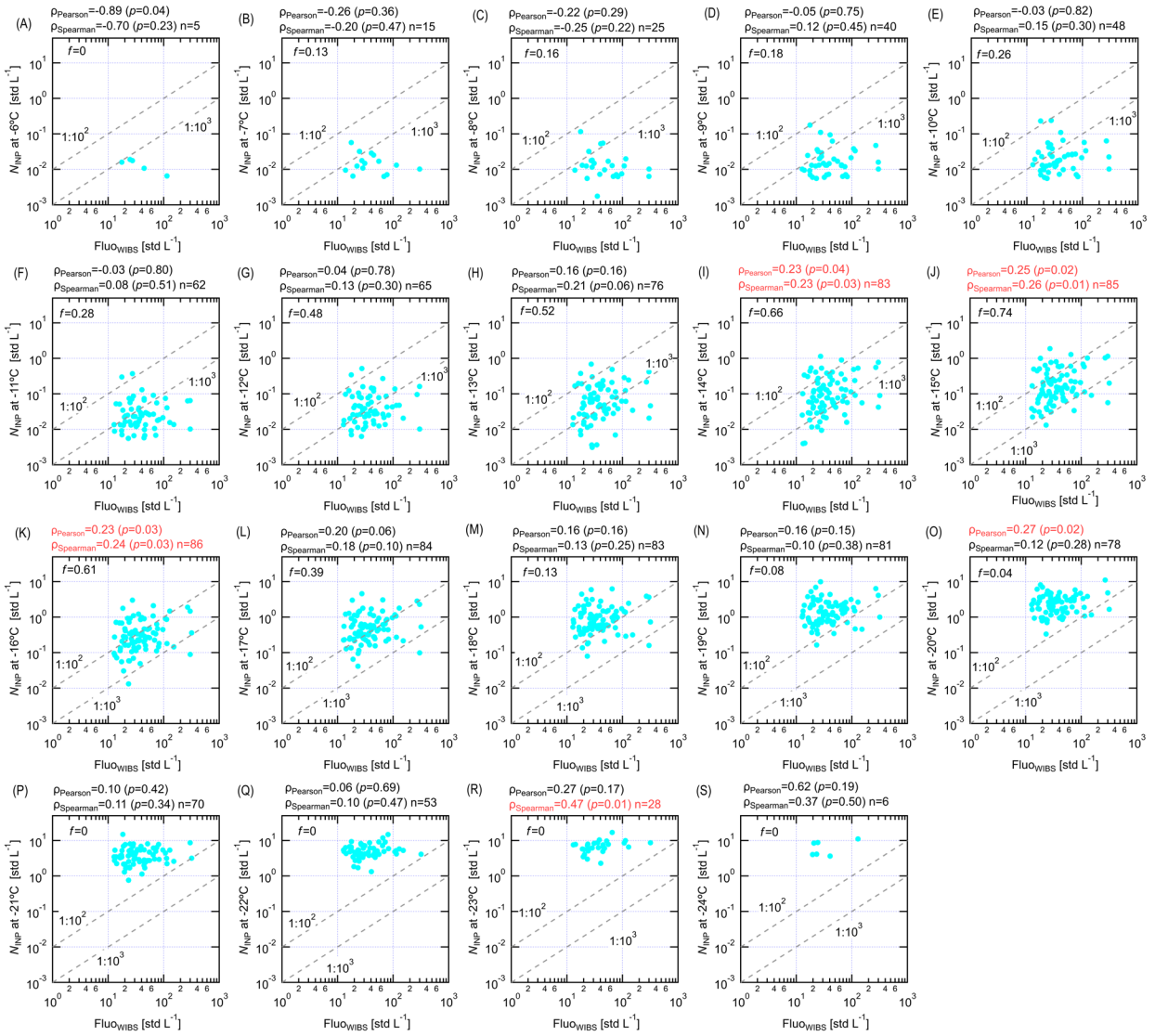

Figure S21. The correlation coefficients ($\rho_{Pearson}$ and $\rho_{Spearman}$) between INP number concentrations at a fixed *T* (on the *x*-axis) for untreated samples and $Fluo_{WIBS}$ particle number concentration. Panels (a) to (s) are for INP number concentrations tested from −6 to −24°C. Both $\rho_{Pearson}$ and $\rho_{Spearman}$ coefficients and corresponding *p* values are provided at the top of each panel. Significant correlations ($p<0.05$) are indicated in red. The *f* value means the fraction of data points within the range specified in the figure.

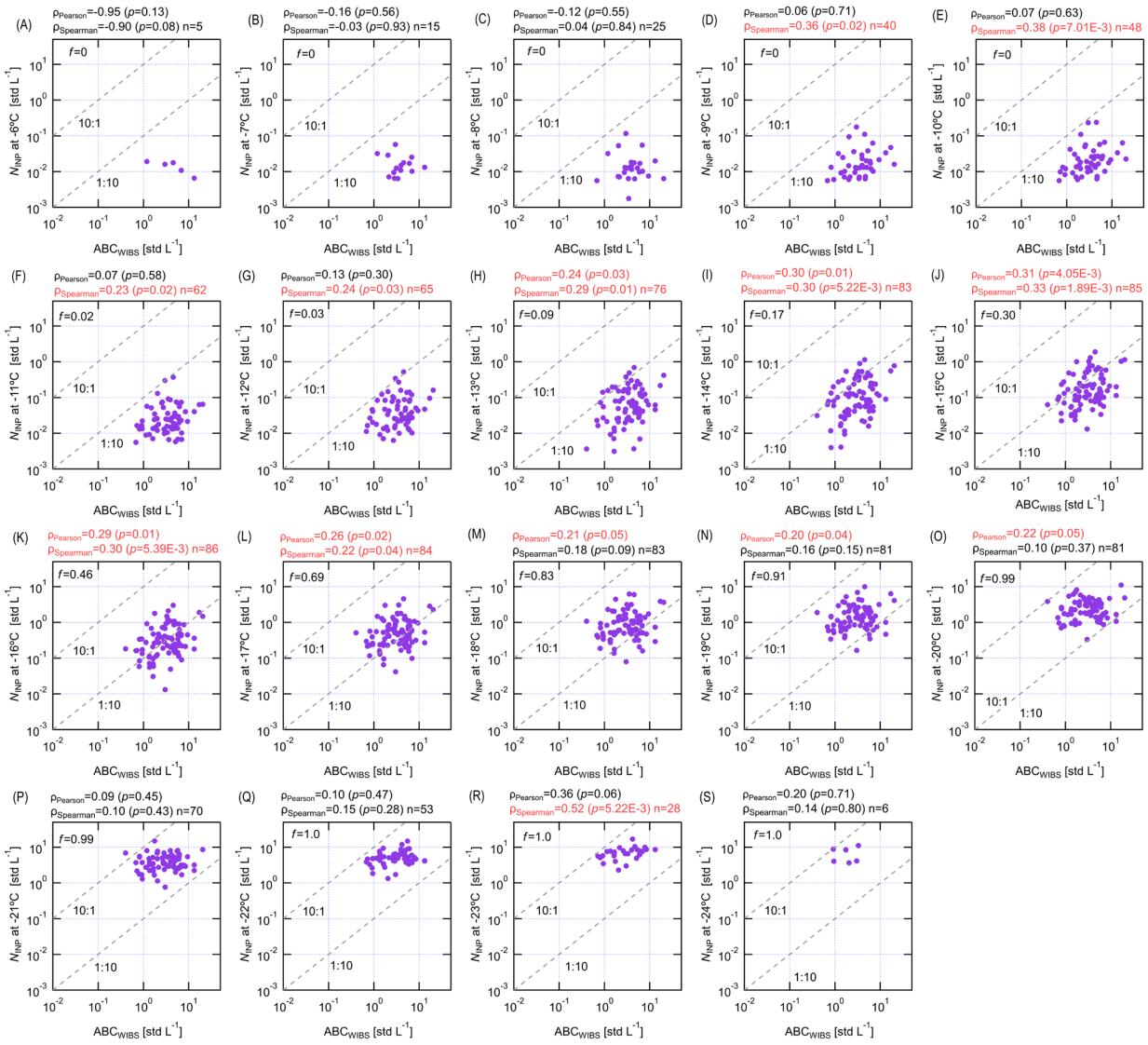

Figure S22. The correlation coefficients ($\rho_{Pearson}$ and $\rho_{Spearman}$) between INP number concentrations at a fixed *T* (on the *x*-axis) for untreated samples and ABC_{WIBS} particle number concentration. Panels (a) to (s) are for INP number concentrations tested from −6 to −24°C. Both $\rho_{Pearson}$ and $\rho_{Spearman}$ coefficients and corresponding *p* values are provided at the top of each panel. Significant correlations ($p<0.05$) are indicated in red. The *f* value means the fraction of data points within the range specified in the figure.

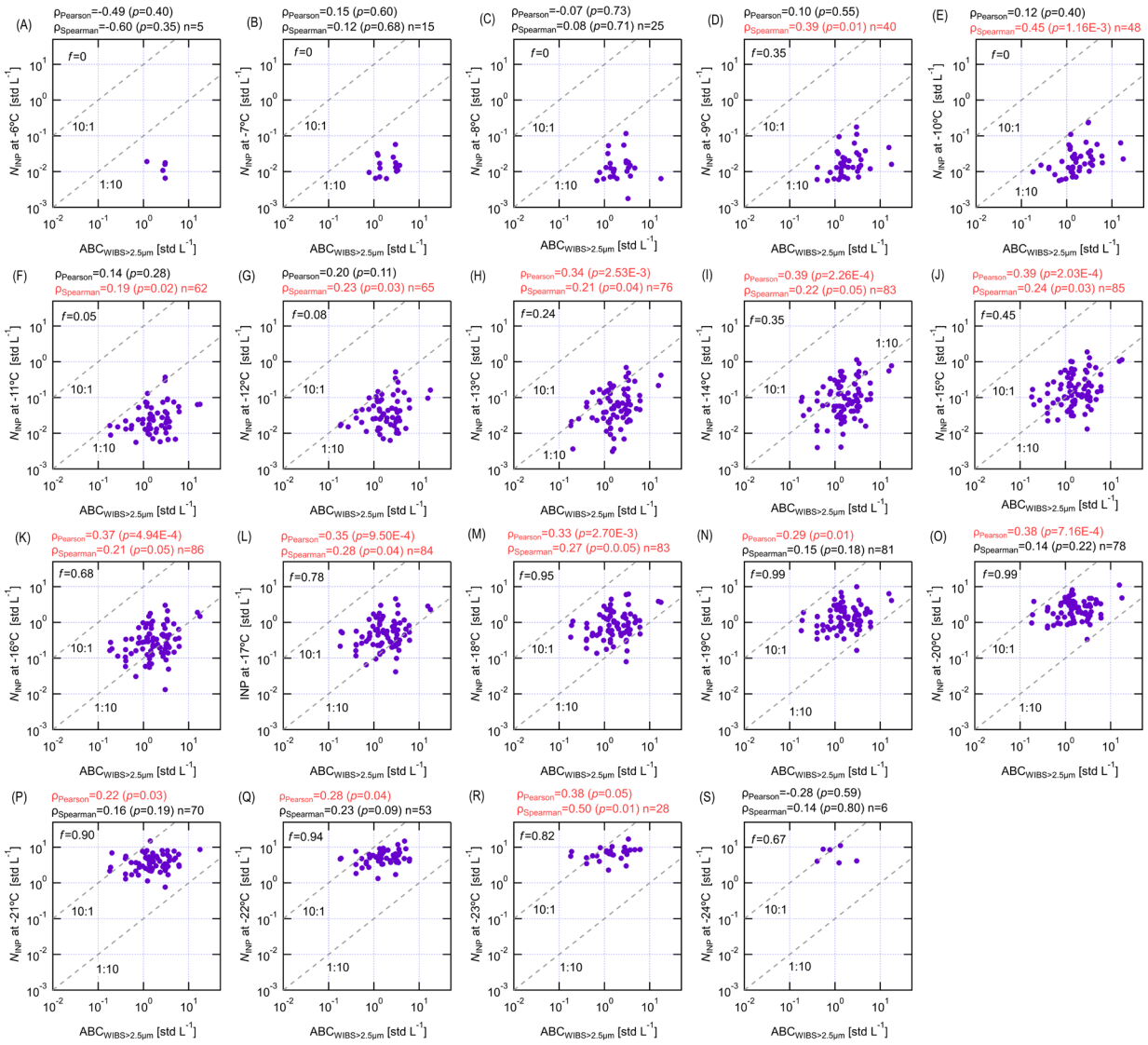

Figure S23. The correlation coefficients ($\rho_{Pearson}$ and $\rho_{Spearman}$) between INP number concentrations at a fixed *T* (on the *x*-axis) for untreated samples and $ABC_{WIBS>2.5\mu m}$ particle number concentration. Panels (a) to (s) are for INP number concentrations tested from −6 to −24°C. Both $\rho_{Pearson}$ and $\rho_{Spearman}$ coefficients and corresponding *p* values are provided at the top of each panel. Significant correlations ($p<0.05$) are indicated in red. The *f* value means the fraction of data points within the range specified in the figure.

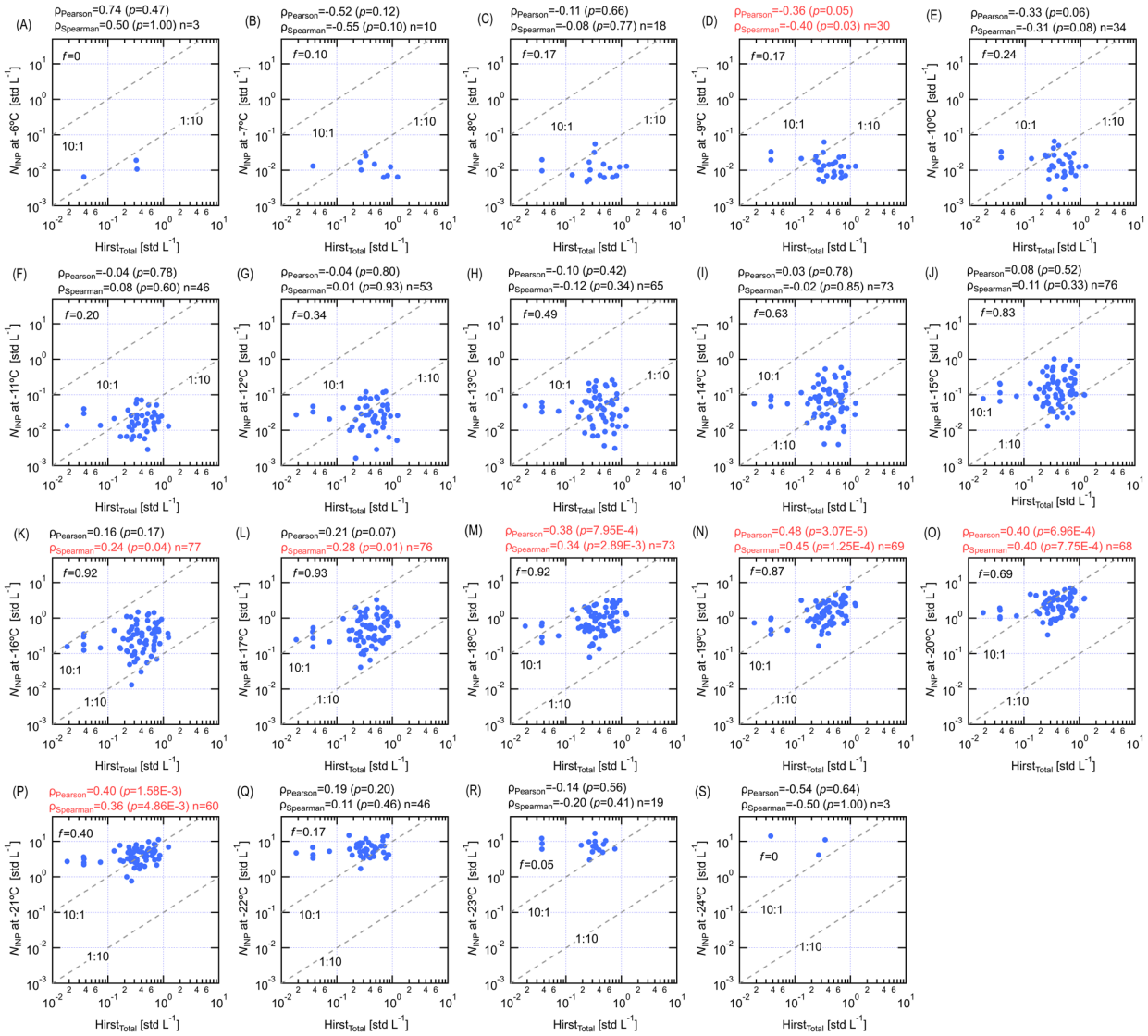

Figure S24. The correlation coefficients ($\rho_{Pearson}$ and $\rho_{Spearman}$) between INP number concentrations at a fixed *T* (on the *x*-axis) for untreated samples and $Hirst_{Total}$ particle number concentration. Panels (a) to (s) are for INP number concentrations tested from −6 to −24°C. Both $\rho_{Pearson}$ and $\rho_{Spearman}$ coefficients and corresponding *p* values are provided at the top of each panel. Significant correlations ($p<0.05$) are indicated in red. The *f* value means the fraction of data points within the range specified in the figure.

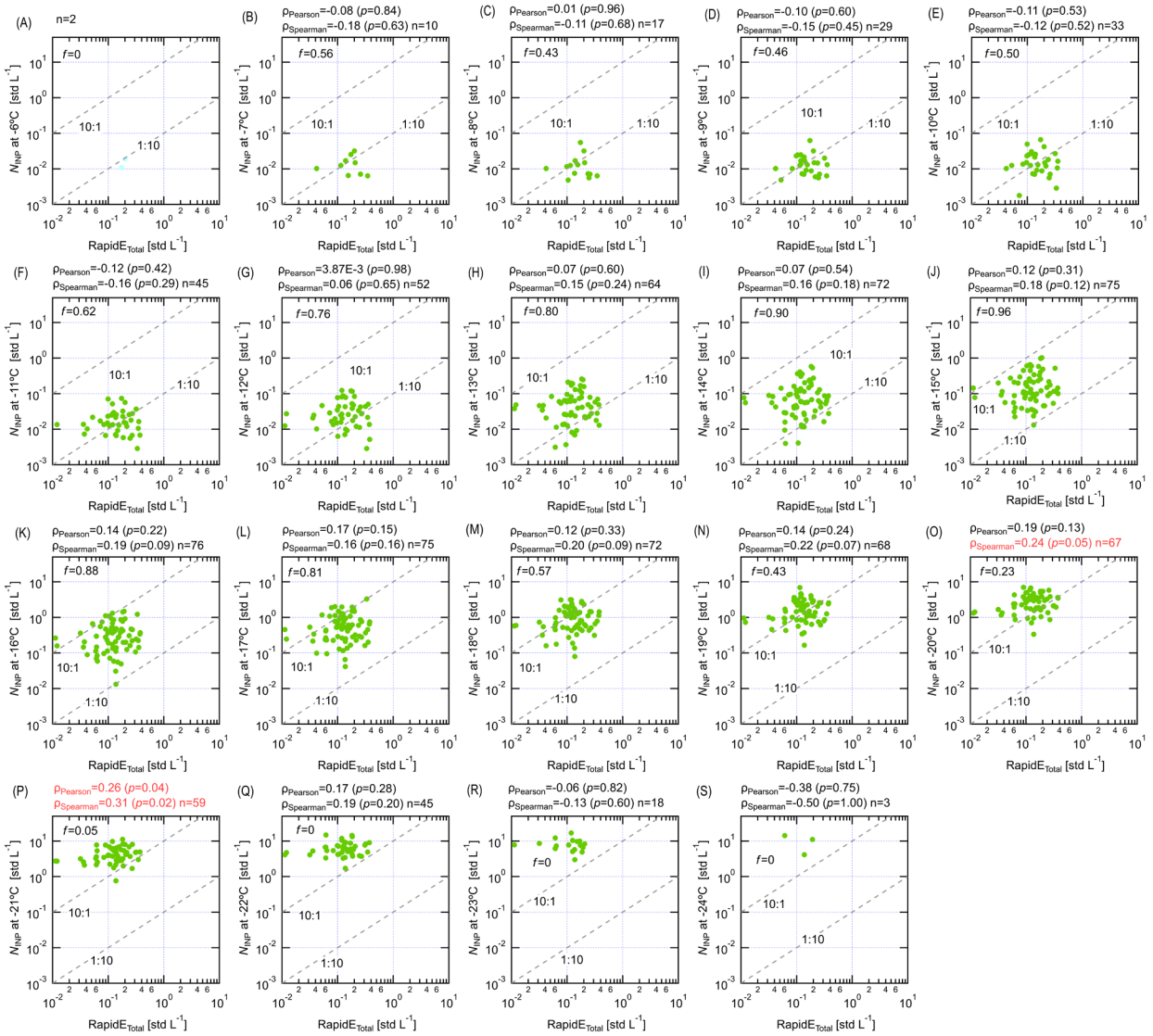

Figure S25. The correlation coefficients ($\rho_{Pearson}$ and $\rho_{Spearman}$) between INP number concentrations at a fixed *T* (on the *x*-axis) for untreated samples and RapidE$_{Total}$ particle number concentration. Panels (a) to (s) are for INP number concentrations tested from −6 to −24°C. Both $\rho_{Pearson}$ and $\rho_{Spearman}$ coefficients and corresponding *p* values are provided at the top of each panel. Significant correlations ($p<0.05$) are indicated in red. The *f* value means the fraction of data points within the range specified in the figure.

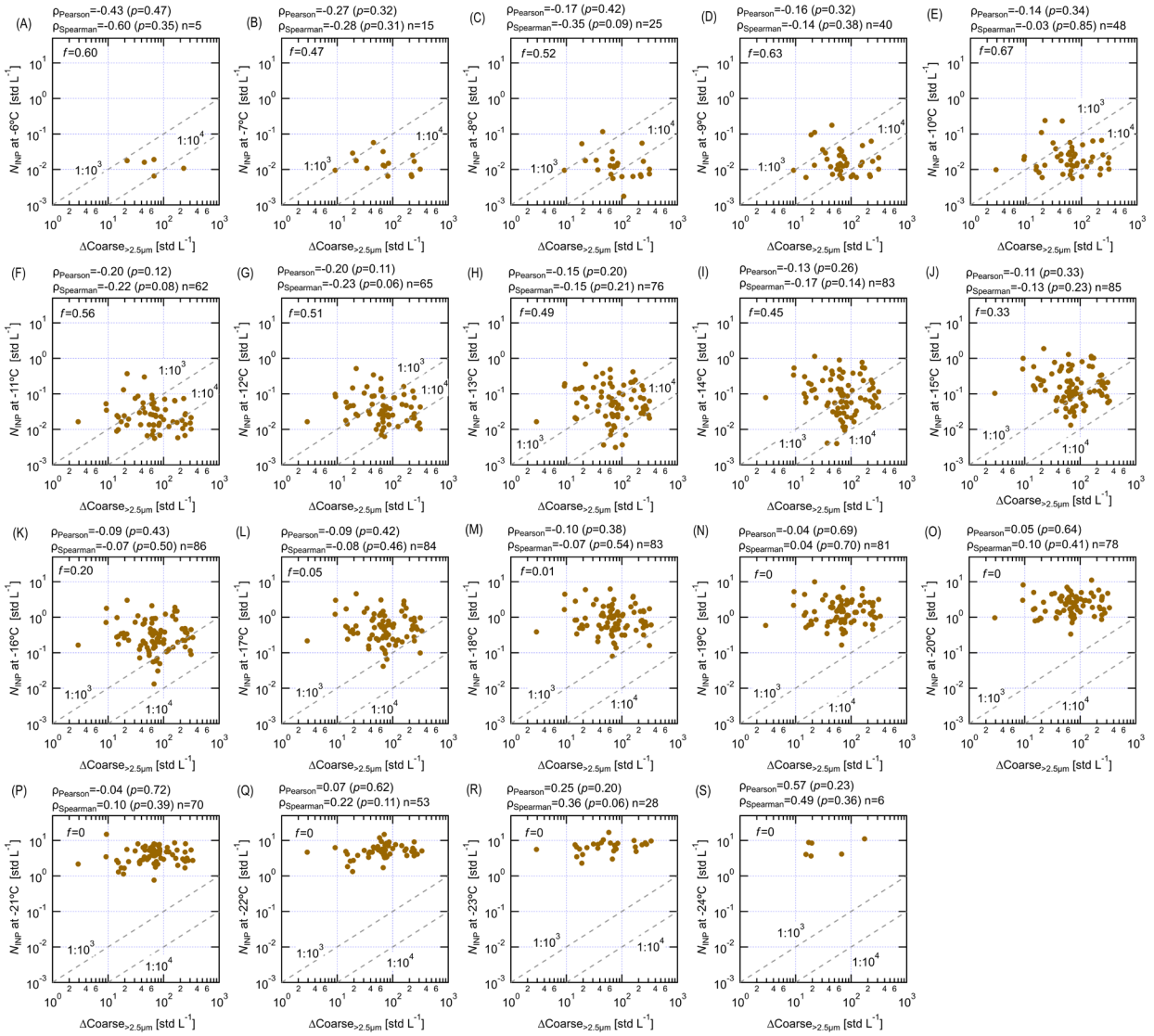

Figure S26. The correlation coefficients ($\rho_{Pearson}$ and $\rho_{Spearman}$) between INP number concentrations at a fixed *T* (on the *x*-axis) for untreated samples and $\Delta Coarse_{>2.5\mu m}$ particle number concentration. Panels (a) to (s) are for INP number concentrations tested from −6 to −24°C. Both $\rho_{Pearson}$ and $\rho_{Spearman}$ coefficients and corresponding *p* values are provided at the top of each panel. Significant correlations ($p<0.05$) are indicated in red. The *f* value means the fraction of data points within the range specified in the figure.

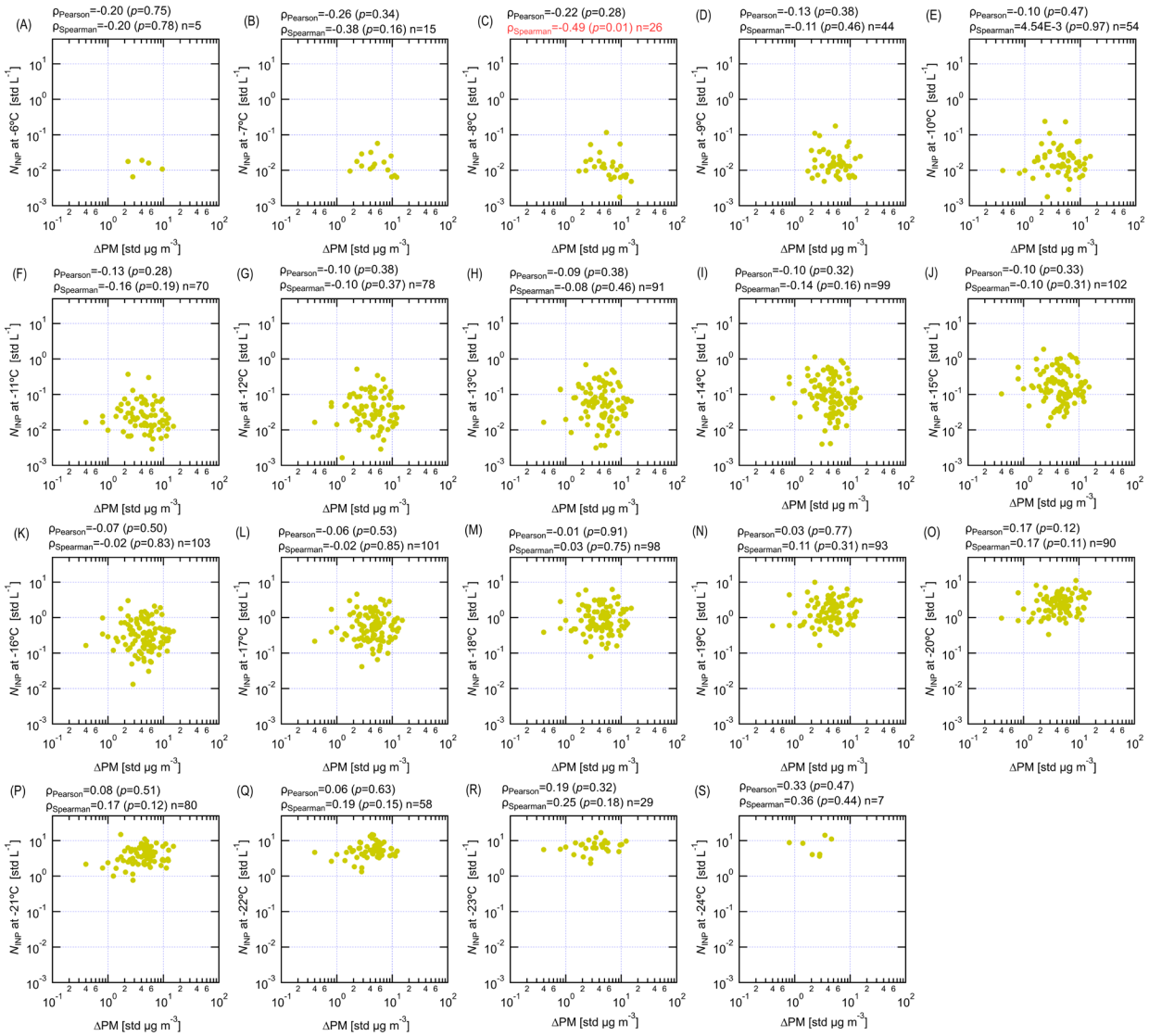

Figure S27. The correlation coefficients ($\rho_{Pearson}$ and $\rho_{Spearman}$) between INP number concentrations at a fixed *T* (on the *x*-axis) for untreated samples and ΔPM particle number concentration. Panels (a) to (s) are for INP number concentrations tested from −6 to −24°C. Both $\rho_{Pearson}$ and $\rho_{Spearman}$ coefficients and corresponding *p* values are provided at the top of each panel. Significant correlations ($p<0.05$) are indicated in red.

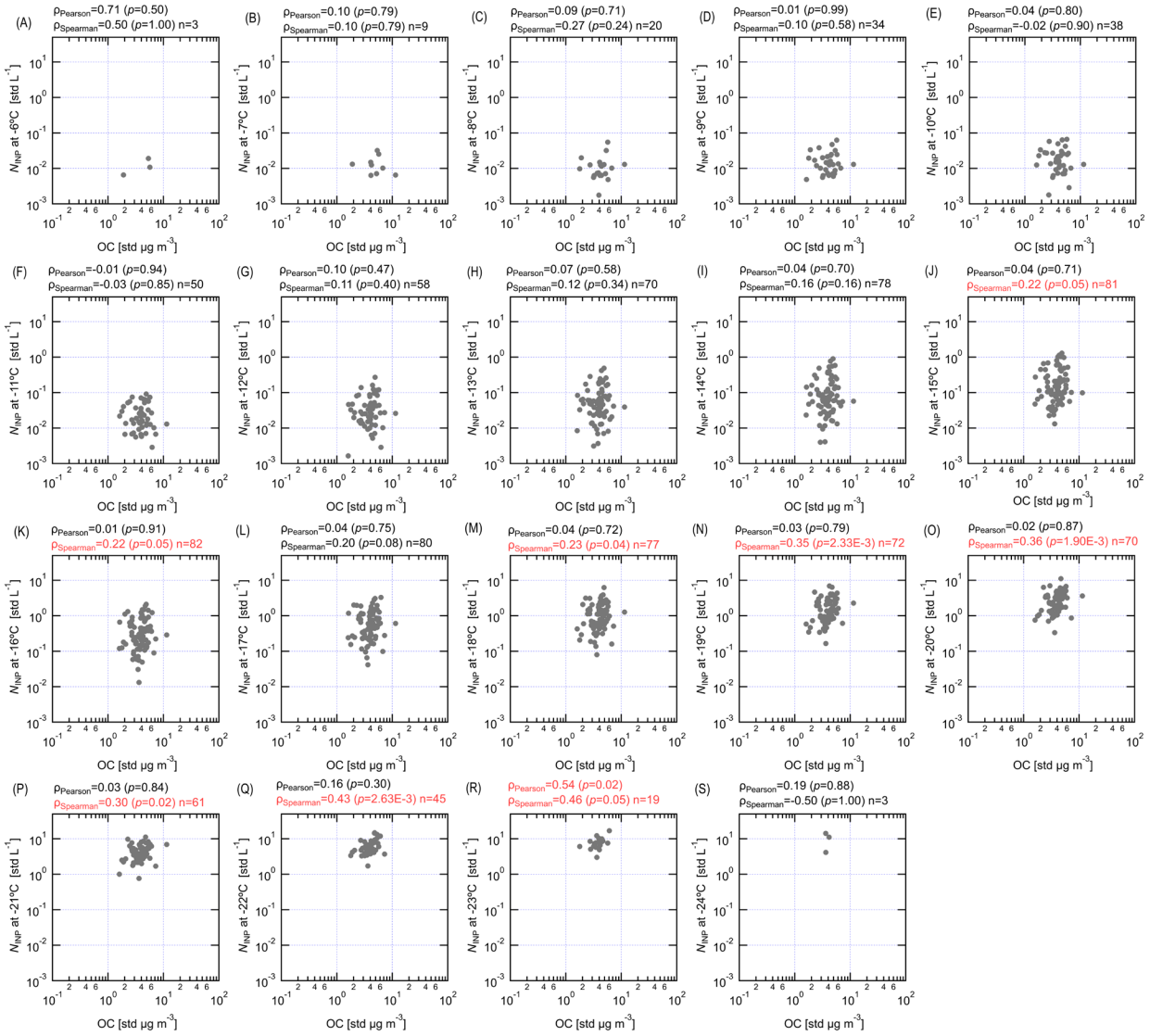

Figure S28. The correlation coefficients ($\rho_{Pearson}$ and $\rho_{Spearman}$) between INP number concentrations at a fixed *T* (on the *x*-axis) for untreated samples and OC particle number concentration. Panels (a) to (s) are for INP number concentrations tested from −6 to −24°C. Both $\rho_{Pearson}$ and $\rho_{Spearman}$ coefficients and corresponding *p* values are provided at the top of each panel. Significant correlations ($p<0.05$) are indicated in red.

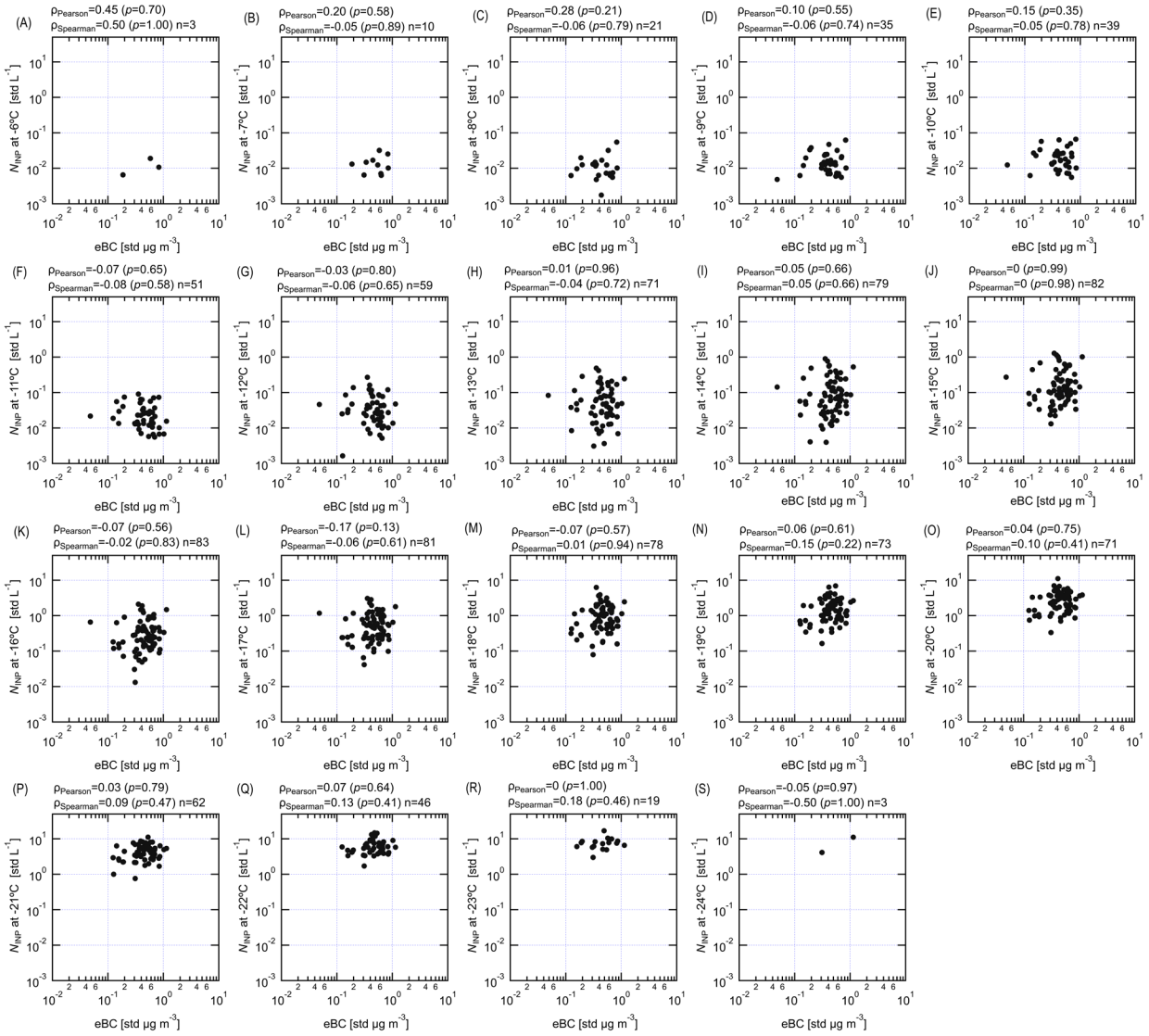

Figure S29. The correlation coefficients ($\rho_{Pearson}$ and $\rho_{Spearman}$) between INP number concentrations at a fixed *T* (on the *x*-axis) for untreated samples and eBC particle number concentration. Panels (a) to (s) are for INP number concentrations tested from −6 to −24°C. Both $\rho_{Pearson}$ and $\rho_{Spearman}$ coefficients and corresponding *p* values are provided at the top of each panel. Significant correlations ($p<0.05$) are indicated in red.

S13 Performance of different parameterizations for individual datasets

Three INP datasets from different regions presented in Figs. 8 and 9 in the main text and Fig. S31 are provided in Fig. S30. Figure S31 presents the predictability of different INP parameterizations including INP-WIBS$_{Fluo}$, INP-WIBS$_{Total}$_1 and INP-WIBS$_{Total}$_2 for individual datasets. The parameters for each case are provided in Table S2. In general, all parameterizations can predict more than 90% (65%) of INP observations in comparison to the true values within a factor of 10 (3). Notably, the results show that the same parameterization perform better for a dataset containing more PBAPs. It is shown that INPs at Payerne (this study) are dominated by PBAPs, PBAPs are a major source for INPs observed at Mt. Helmos (Gao et al., 2024) and PBAPs are relevant but not necessarily the primary INP source for INPs observed at Ay-Ålesund (Li et al., 2023). Thus, the importance and dominance of PBAPs in different campaigns may follow the order as Payerne, Mt. Helmos and Ny-Ålesund. The same INP parameterization in Fig. S31 shows slightly decreased predictability also in a similar order sowing decreasing f_{10} from approximately 100% to 92%. In brief, the results may suggest the presented parameterizations in Fig. S31 may be more suitable for field sites that are rich in PBAPs.

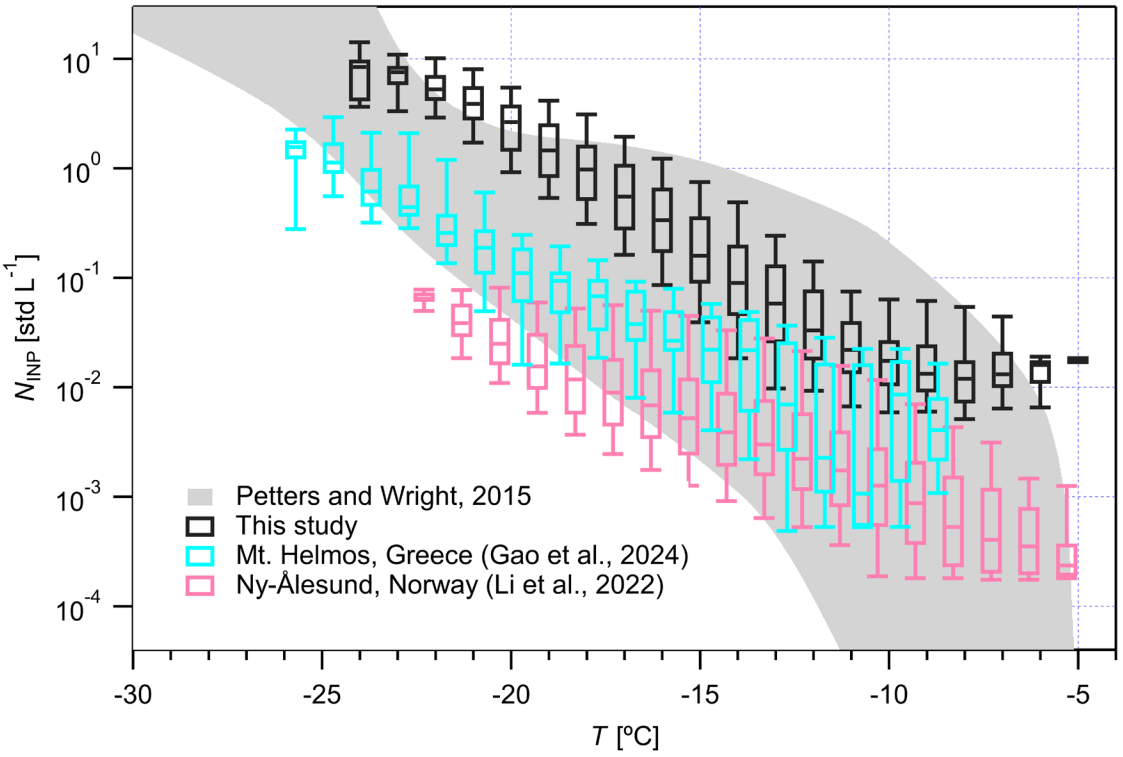

Figure S30. INP dataset included in INP-WIBS parameterizations presented in Figs. 8 and 9 in the main text and Fig. S27. The grey shading shows an global envelope reported by Petters and Wright (2015). Observations in three field campaigns at Payerne in Switzerland (this study), Mt. Helmos in Greece (Gao et al., 2024) and Ny-Ålesund in Norway (Li et al., 2022), are presented by box plots. Each box presents data points in a *T* interval of 1°C. The box shows the median line and the range between 25th and 75th quartiles. The lower and upper caps of the box indicate the 9th and 91th percentiles, respectively. Boxes are offset by −0.3°C for legibility.

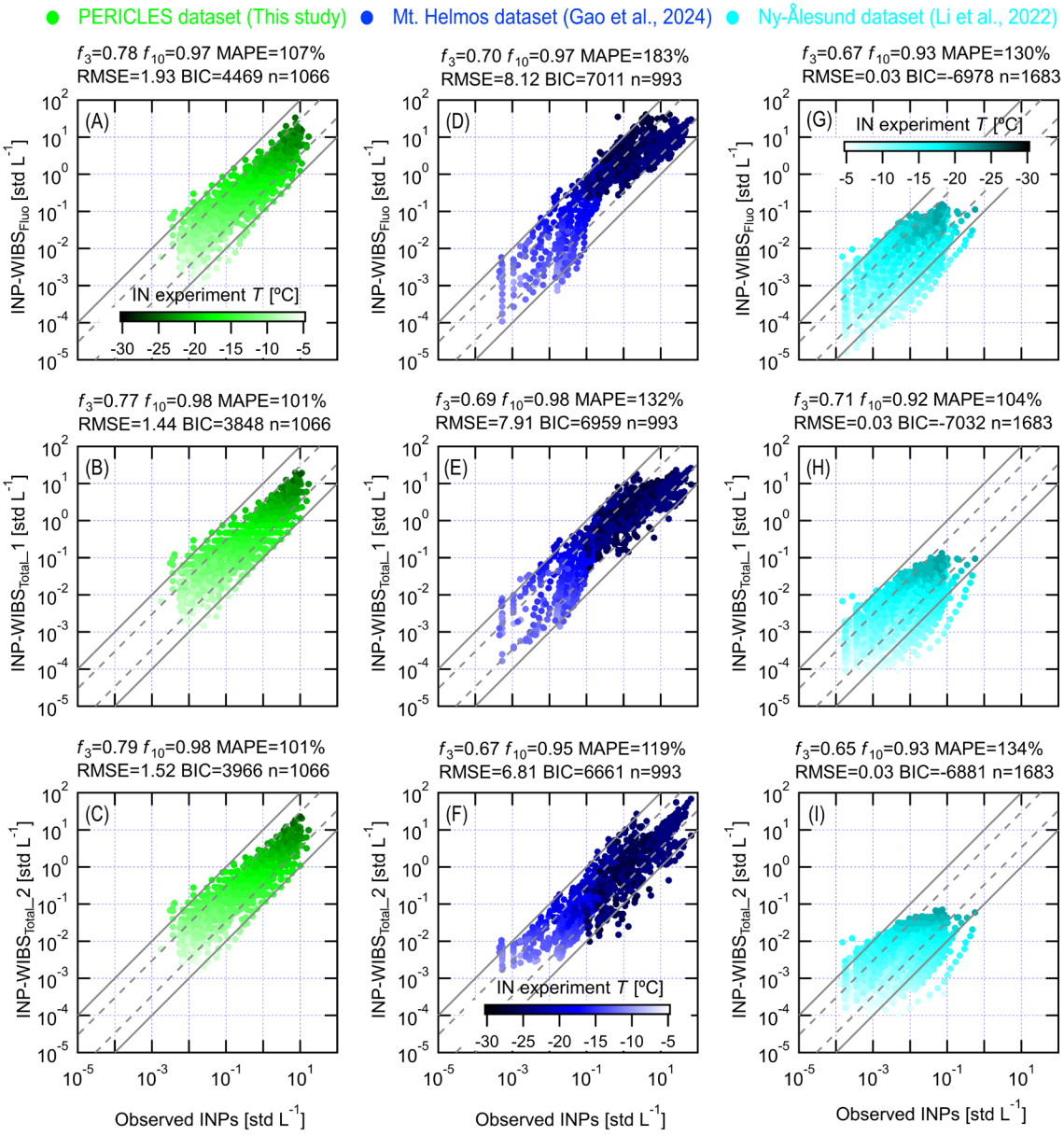

Figure S31. The performance of different parameterizations with parameters calculated from different datasets (PERICLES, Mt. Helmos and Ny-Ålesund). (a), (b) and (c) INP-WIBS$_{Fluo}$, INP-WIBS$_{Total}$_1 and INP-WIBS$_{Total}$_2 parameterizations for PERICLES dataset, respectively. (d), (e) and (f) INP-WIBS$_{Fluo}$, INP-WIBS$_{Total}$_1 and INP-WIBS$_{Total}$_2 parameterizations for Mt. Helmos dataset, respectively. (g), (h) and (i) INP-WIBS$_{Fluo}$, INP-WIBS$_{Total}$_1 and INP-WIBS$_{Total}$_2 parameterizations for Ny-Ålesund dataset, respectively. The temperature condition for INP data is scaled to the colour bar. Note that parameterizations based on the same dataset use the same colour bar. The dashed lines confine the range for observed and predicted data points within a factor of 3. The fraction of observed and predicted data points within a factor of 3 (f_3) and 10 (f_{10}) is provided in each

panel, respectively. MAPE stands for mean absolute percentage error. RMSE is the root-mean-square error used as a measure of the difference between observed and predicted data. BIC is a value calculated by applying the Bayesian information criteria to evaluate the goodness of parameterizations based on the same dataset (Schwarz, 1978). The *n* value shows the number of observed data points.

Table S2. Parameters for INP-WIBS parameterizations with different datasets.

INP Parameterizations	Formulation	PERICLES dataset (This study)	Mt. Helmos dataset (Gao et al., 2024)	Ny-Ålesund dataset (Li et al., 2022)
$WIBS_{Fluo}$	$N_{INP} = \exp(aT+b) * (Fluo_{WIBS}/1000)^{(cT+d)} * (WIBS_{ratio})^{(eT+f)}$	a = −0.0290 b = −2.5000 c = −0.0140 d = −0.0600 e = 0.0915 f = 1.4000	a = −0.096725 b = −3.6932 c = −0.16288 d = −3.04 e = 0.024358 f = 0.44052	a = −0.4691 b = −10.7954 c = 0.0812 d = 1.6788 e = 0.0916 f = 2.6489
$WIBS_{Total}\_1$	$N_{INP} = \exp(aT+b) * Total_{WIBS}^{(cT+d)} * (WIBS_{ratio} * e + f)$	a = 0.1800 b = −15.8500 c =−0.0800 d =−1.3800 e =6.0E7 f = 9.0E7	a =0.45678 b = −3.456 c =−0.15 d =−2.7989 e =220000 f = 18400	a = −0.0901 b = −14.8585 c = −0.0488 d = −0.6516 e = 20041 f = 539
$WIBS_{Total}\_2$	$N_{INP} = a(-T)^{b} * Total_{WIBS}^{(cT+d)} * \left(\frac{1}{WIBS_{ratio} * e + f}\right)$	a =−48 b = 0.28 c = −0.0560 d = −0.80 e = 9000 f = −880	a =−4244444.44 b = −5.5 c = −0.119 d = −1.69 e = 641.55 f = −154.31	a = −215.5457 b = −0.1511 c = −0.0531 d = −1.070 e = 297 f = −10410

References

Coluzza, I., Creamean, J., Rossi, M., Wex, H., Alpert, P., Bianco, V., Boose, Y., Dellago, C., Felgitsch, L., Fröhlich-Nowoisky, J., Herrmann, H., Jungblut, S., Kanji, Z., Menzl, G., Moffett, B., Moritz, C., Mutzel, A., Pöschl, U., Schauperl, M., Scheel, J., Stopelli, E., Stratmann, F., Grothe, H., and Schmale, D.: Perspectives on the Future of Ice Nucleation Research: Research Needs and Unanswered Questions Identified from Two International Workshops, Atmos., 8, https://doi.org/10.3390/atmos8080138, 2017.

Conen, F., Einbock, A., Mignani, C., and Hüglin, C.: Measurement report: Ice-nucleating particles active ≥ −15 °C in free tropospheric air over western Europe, Atmos. Chem. Phys., 22, 3433-3444, https://doi.org/10.5194/acp-22-3433-2022, 2022.

David, R. O., Cascajo-Castresana, M., Brennan, K. P., Rösch, M., Els, N., Werz, J., Weichlinger, V., Boynton, L. S., Bogler, S., Borduas-Dedekind, N., Marcolli, C., and Kanji, Z. A.: Development of the DRoplet Ice Nuclei Counter Zurich (DRINCZ): Validation and Application to Field-Collected Snow Samples, Atmos. Meas. Tech., 12, 6865-6888, https://doi.org/10.5194/amt-12-6865-2019, 2019.

Gao, K., Vogel, F., Foskinis, R., Vratolis, S., Gini, M. I., Granakis, K., Billault-Roux, A.-C., Georgakaki, P., Zografou, O., Fetfatzis, P., Berne, A., Papagiannis, A., Eleftheridadis, K., Möhler, O., and Nenes, A.: Biological and dust aerosol as sources of ice nucleating particles in the Eastern Mediterranean: source apportionment, atmospheric processing and parameterization, Atmos. Chem. Phys., 24, 9939-9974, https://doi.org/10.5194/acp-24-9939-2024, 2024.

Huffman, J. A., Prenni, A. J., DeMott, P. J., Pöhlker, C., Mason, R. H., Robinson, N. H., Fröhlich-Nowoisky, J., Tobo, Y., Després, V. R., Garcia, E., Gochis, D. J., Harris, E., Müller-Germann, I., Ruzene, C., Schmer, B., Sinha, B., Day, D. A., Andreae, M. O., Jimenez, J. L., Gallagher, M., Kreidenweis, S. M., Bertram, A. K., and Pöschl, U.: High concentrations of biological aerosol particles and ice nuclei during and after rain, Atmos. Chem. Phys., 13, 6151-6164, https://doi.org/10.5194/acp-13-6151-2013, 2013.

Lacher, L., Clemen, H.-C., Shen, X., Mertes, S., Gysel-Beer, M., Moallemi, A., Steinbacher, M., Henne, S., Saathoff, H., Möhler, O., Höhler, K., Schiebel, T., Weber, D., Schrod, J., Schneider, J., and Kanji, Z. A.: Sources and nature of ice-nucleating particles in the free troposphere at Jungfraujoch in winter 2017, Atmos. Chem. Phys., https://doi.org/10.5194/acp-21-16925-2021, 2021.

Li, G., Wieder, J., Pasquier, J. T., Henneberger, J., and Kanji, Z. A.: Predicting atmospheric background number concentration of ice nucleating particles in the Arctic, Atmospheric Chemistry and Physics Discussions, https://doi.org/10.5194/acp-2022-21, 2022.

Li, G., Wilbourn, E. K., Cheng, Z., Wieder, J., Fagerson, A., Henneberger, J., Motos, G., Traversi, R., Brooks, S. D., Mazzola, M., China, S., Nenes, A., Lohmann, U., Hiranuma, N., and Kanji, Z. A.: Physicochemical characterization and source apportionment of Arctic ice-nucleating particles observed in Ny-Ålesund in autumn 2019, Atmos. Chem. Phys., 23, 10489-10516, https://doi.org/10.5194/acp-23-10489-2023, 2023.

Mignani, C., Wieder, J., Sprenger, M. A., Kanji, Z. A., Henneberger, J., Alewell, C., and Conen, F.: Towards parameterising atmospheric concentrations of ice-nucleating particles active at moderate supercooling, Atmos. Chem. Phys., 21, 657-664, https://doi.org/10.5194/acp-21-657-2021, 2021.

Petters, M. D. and Wright, T. P.: Revisiting ice nucleation from precipitation samples, Geophys. Res. Lett., 42, 8758-8766, https://doi.org/10.1002/2015gl065733, 2015.

Prenni, A. J., Tobo, Y., Garcia, E., DeMott, P. J., Huffman, J. A., McCluskey, C. S., Kreidenweis, S. M., Prenni, J. E., Pöhlker, C., and Pöschl, U.: The impact of rain on ice nuclei populations at a forested site in Colorado, Geophys. Res. Lett., 40, 227-231, https://doi.org/10.1029/2012gl053953, 2013.
Schneider, J., Höhler, K., Heikkilä, P., Keskinen, J., Bertozzi, B., Bogert, P., Schorr, T., Umo, N. S., Vogel, F., Brasseur, Z., Wu, Y., Hakala, S., Duplissy, J., Moisseev, D., Kulmala, M., Adams, M. P., Murray, B. J., Korhonen, K., Hao, L., Thomson, E. S., Castarède, D., Leisner, T., Petäjä, T., and Möhler, O.: The seasonal cycle of ice-nucleating particles linked to the abundance of biogenic aerosol in boreal forests, Atmos. Chem. Phys., 21, 3899-3918, https://doi.org/10.5194/acp-21-3899-2021, 2021.
Schwarz, G.: Estimating the Dimension of a Model, The Annals of Statistics, 6, 461-461, https://doi.org/10.1214/aos/1176344136, 1978.
Wieder, J., Mignani, C., Schär, M., Roth, L., Sprenger, M., Henneberger, J., Lohmann, U., Brunner, C., and Kanji, Z. A.: Unveiling atmospheric transport and mixing mechanisms of ice-nucleating particles over the Alps, Atmos. Chem. Phys., 22, 3111-3130, https://doi.org/10.5194/acp-22-3111-2022, 2022.